



# Photometric Redshifts of Galaxies

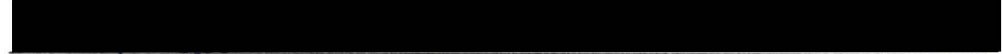
by  
Stephen Donald Jermy Gwyn  
B.Sc. McGill 1990

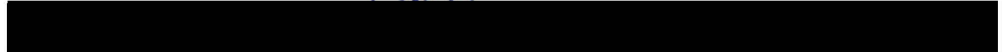
A Thesis Submitted in Partial Fulfillment of the  
Requirements for the Degree of  
MASTER OF SCIENCE  
in the Department of Physics and Astronomy


We accept this thesis as conforming  
to the required standard.

  
Dr. F. D. A. Hartwick, Supervisor (Department of Physics & Astronomy)

  
Dr. C. J. Pritchett, Departmental Member (Department of Physics & Astronomy)

  
Dr. J. B. Tatum, Departmental Member (Department of Physics & Astronomy)

  
Dr. K. R. Dixon, Outside Member (Department of Chemistry)

  
Dr. D. Crampton, External Examiner (Dominion Astrophysical Observatory)

© Stephen Donald Jermy Gwyn, 1995,  
University of Victoria.

*All rights reserved. Thesis may not be reproduced in whole or in part,  
by mimeograph or other means, without the permission of the author.*

QB135


G9


Supervisor: Dr. F. D. A. Hartwick


## Abstract


This thesis presents a method to measure the redshifts,  $z$ , of galaxies using broadband photometry. In this method, the photometry of observed galaxies is converted into low resolution spectral energy distributions by converting  $BVRI$  magnitudes into fluxes. Template galaxy spectra are obtained by redshifting the spectra of local galaxies. Redshifts are determined by comparing the observed spectral energy distributions to these templates. Photometric data for galaxies of known spectroscopic redshift were obtained at the Canada France Hawaii Telescope to test the accuracy of this method. It was found that, if the templates are modified for evolution using either theoretical models or empirical corrections, the accuracy improves. With these modifications, the method is accurate to  $\Delta z = \pm 0.125$ . The efficacy and speed with which the properties of a large number of galaxies can be determined using photometric redshifts was demonstrated by measuring the luminosity function for a sample of 187 moderate redshift ( $\langle z \rangle = .34$ ) galaxies


Examiners:

  
Dr. F. D. A. Hartwick, Supervisor (Department of Physics & Astronomy)

  
Dr. C. J. Pritchett, Departmental Member (Department of Physics & Astronomy)

  
Dr. J. B. Tatum, Departmental Member (Department of Physics & Astronomy)

  
Dr. K. R. Dixon, Outside Member (Department of Chemistry)

  
Dr. D. Crampton, External Examiner (Dominion Astrophysical Observatory)

# Contents

<b>Abstract</b>	<b>ii</b>
<b>Contents</b>	<b>iii</b>
<b>List of Tables</b>	<b>v</b>
<b>List of Figures</b>	<b>vi</b>
<b>Acknowledgements</b>	<b>vii</b>
<b>1 Introduction</b>	<b>1</b>
<b>2 Previous work</b>	<b>5</b>
2.1 Baum . . . . .	5
2.2 Koo . . . . .	6
2.3 Loh and Spillar . . . . .	7
<b>3 Data</b>	<b>9</b>
3.1 Observations . . . . .	9
3.2 Image Reductions . . . . .	10
3.3 Photometry . . . . .	12
<b>4 Basic technique</b>	<b>21</b>
4.1 Photometry to spectral energy distributions . . . . .	22
4.2 The template spectra . . . . .	24
4.3 Comparing the templates to the SED's . . . . .	33
4.4 Results . . . . .	34

CONTENTS

iv

<b>5 Evolution</b>	<b>40</b>
5.1 Theoretical evolution . . . . .	41
5.2 Empirical evolution . . . . .	44
5.3 Error distributions . . . . .	51
<b>6 Luminosity functions</b>	<b>59</b>
6.1 The sample . . . . .	59
6.2 The $1/V_a$ method . . . . .	60
6.3 The luminosity function . . . . .	61
<b>7 Conclusion</b>	<b>64</b>
7.1 Summary . . . . .	64
7.2 Future work . . . . .	65
<b>Bibliography</b>	<b>71</b>
<b>Glossary</b>	<b>73</b>

# List of Tables

3.1	List of observations . . . . .	11
3.2	The Colless galaxies: Part 1 . . . . .	13
3.3	The Colless galaxies: Part 2 . . . . .	14
3.4	Photometry for the Colless galaxies: Part 1 . . . . .	17
3.5	Photometry for the Colless galaxies: Part 2 . . . . .	18
3.6	The galaxies used for developing the photometric redshift technique: Part 1 . . . . .	19
3.7	The galaxies used for developing the photometric redshift technique: Part 2 . . . . .	20
4.1	Filter properties . . . . .	23
4.2	Spectral morphologies . . . . .	28
4.3	Results from the basic photometric redshift technique: Part 1 . . . . .	38
4.4	Results from the basic photometric redshift technique: Part 2 . . . . .	39
5.1	Additional photometric and redshift data . . . . .	51

# List of Figures

4.1	<i>BVRI</i> photometry converted into a spectral energy distribution	25
4.2	The spectra of elliptical and irregular galaxies . . . . .	26
4.3	The spectrum of an Sb galaxy . . . . .	29
4.4	An example of a redshifted spectrum . . . . .	30
4.5	An example of a reduced spectrum . . . . .	32
4.6	An example of a galaxy-template comparison . . . . .	35
4.7	Another example of a galaxy-template comparison . . . . .	36
4.8	The trend of $\Delta z$ with spectroscopic redshift . . . . .	37
5.1	The spectral evolution of galaxies . . . . .	43
5.2	$\Delta z$ vs. $z_{spec}$ after theoretical corrections for evolution . . . . .	45
5.3	$F_B/F_V$ as a function of $m$ and $z$ . . . . .	47
5.4	$\Delta z$ vs. $z_{spec}$ for the empirically corrected templates . . . . .	50
5.5	Possible error distributions . . . . .	54
5.6	Simulation results . . . . .	56
6.1	The $B$ luminosity function for medium redshifts . . . . .	63
7.1	The effect of photometric errors on redshift errors . . . . .	68

# Acknowledgements

This research has made use of data obtained from the Canada France Hawaii Telescope (CFHT), which is operated by the National Research Council of Canada, the Centre National de la Recherche Scientifique of France and the University of Hawaii. I would like to thank Dr. Hartwick and Dr. Pritchett for allowing me to use many precious hours of their CFHT observing run.

I gratefully acknowledge les fonds pour la formation de chercheurs et l'aide à la recherche (Fonds FCAR) of the Quebec government for their financial support during the first 5 semesters of this degree.

Many thanks are due to my fellow graduate students, especially M. Luc Simard, for many useful conversations, occasionally on the subject of astronomy. Reverence must be paid to that nectar, coffee, and ambrosia, chocolate. Although this thesis would have been possible without them, it would not have been as pleasant.

I would especially like to thank my supervisor, Dr. Hartwick. Without his financial support and the innumerable discussions in which he supplied guidance, advice and an unfailing pen, this thesis would have been impossible. Without his constant exhortations to further accomplishments, the scope of this thesis would have been severely reduced.

# Chapter 1

## Introduction

As a result of the expansion of the universe, almost all the galaxies in the sky appear to be receding from us. As they do so, the light coming from them is said to be *redshifted*. The wavelength of each photon is lengthened or shifted towards the red end of the spectrum. The fractional amount of shift is known as the *redshift*, denoted  $z$ , of the galaxy. If  $\lambda_0$  is the rest wavelength of a photon coming from a receding galaxy, and  $\lambda$  is the wavelength of the same photon as measured by us, then the redshift is:

$$z = \frac{\lambda - \lambda_0}{\lambda_0}. \quad (1.1)$$

Through the Hubble law, the redshift of a galaxy is proportional to its distance in megaparsecs,  $d$ , at least at small redshifts:

$$d = \frac{cz}{H_0} \quad (1.2)$$

where  $c$  is the speed of light in  $\text{km sec}^{-1}$  and  $H_0$  is the Hubble constant, which, in this thesis, is assumed to be  $75 \text{ km sec}^{-1} \text{ Mpc}^{-1}$ . For larger redshifts the

exact relationship is

$$d_L = \frac{c}{H_0 q_0^2} \{q_0 z + (q_0 - 1)[(1 + 2q_0 z)^{1/2} - 1]\}, \quad (1.3)$$

where  $q_0$  is the deceleration parameter and  $d_L$  is now the luminosity distance. Since the distance to most galaxies cannot be measured, either equation 1.2 or 1.3 must be used to get an estimate of the distance. Knowing the distance to a galaxy is important because it allows one to deduce the actual properties of a galaxy (absolute magnitude, size...) from the observable properties (apparent magnitude, angular size...).

In general, the redshift of a galaxy is measured spectroscopically. The spectrum of the galaxy is observed and recorded. Lines, generally emission lines, are identified and their wavelengths measured. The measured wavelengths are compared with the rest wavelengths using equation 1.1 to determine the redshift.

This thesis presents a method to measure the redshifts of galaxies using broad-band *BVRI* photometry instead of spectroscopy. Rather than observing narrow spectral features of galaxy spectra, such as lines, the photometric redshift technique concentrates on broad features, such as the 4000Å break and the overall shape of a spectrum. In this method, the photometry of observed galaxies is converted into low resolution spectral energy distributions (SED's). Redshifts are determined by comparing these SED's to redshifted template galaxy spectra.

The chief advantage of using the photometric redshift technique is speed. In spectroscopy, the light from the galaxy is separated into narrow wavelength bins a few angstroms across. Each bin then receives only a small

fraction of the total light from the galaxy. Hence, to achieve a sufficiently high signal-to-noise ratio in each bin, long integration times are required. For photometry, however, the bins are much larger, typically  $1000\text{\AA}$  wide. It requires only a short exposure time to reach the same signal-to-noise ratio. Further, imaging detectors usually cover a greater area of the sky than multi-object spectrographs. This means that the redshifts of more objects can be measured simultaneously by using photometry than by spectroscopy.

The main disadvantage of photometric redshifts is its lesser precision. Redshifts measured spectroscopically have uncertainties on the order of  $\Delta z = \pm 0.001$ , while photometric redshift uncertainties are typically  $\Delta z = \pm 0.1$ . For studying individual galaxies, this is a less than useful level of uncertainty. For determining properties of large numbers of galaxies, however, this uncertainty is quite tolerable. Loh and Spillar (1986b; 1986a) used photometric redshifts to measure the density parameter,  $\Omega_0$ . It is also possible to use photometric redshifts to estimate the luminosity function (space density as a function of absolute magnitude) of galaxies.

In order to develop the photometric redshift method, a database of multi-colour photometry and spectroscopic redshifts was needed. Such a database did not exist, so it was necessary to obtain *BVRI* photometry for galaxies of known spectroscopic redshift. The observations at the Canada France Hawaii Telescope and the subsequent data reductions are outlined and the resulting photometry is presented in Chapter 3.

Chapter 4 describes in detail the photometric redshift technique. The initial, somewhat unsatisfactory, results of the technique are shown.

In Chapter 5, the effects of evolution of the spectral energy distributions

of galaxies with look-back time on the photometric redshift technique are discussed and some modifications to the technique are tested.

Chapter 6 demonstrates the usefulness of photometric redshifts. A luminosity function is presented for a sample of 200 galaxies with an average redshift of  $z \sim .3$  calculated using photometric redshifts.

Finally, the findings of this work are summarized and the future of photometric redshifts is discussed in Chapter 7.

But first, Chapter 2 of this thesis outlines a brief history of photometric redshifts.

# Chapter 2

## Previous work

The concept of photometric redshifts is not new. This section will outline a brief history of the photometric redshifts. The list of papers reviewed here is not exhaustive; however, it does cover most of the development of the technique.

### 2.1 Baum

Baum (1962) was the first to develop a technique for measuring redshifts photometrically. He used a photoelectric photometer and 9 bandpasses spanning the spectrum from  $3730\text{\AA}$  to  $9875\text{\AA}$ . With this system he observed the spectral energy distribution (SED) of 6 bright elliptical galaxies in the Virgo cluster. He then observed 3 elliptical galaxies in another cluster (C10925+2044, also known as Abell 0801). By plotting the average SED of the Virgo galaxies and the average SED of the C10925 galaxies on the same graph using a logarithmic wavelength scale, he was able to measure the displacement between the two energy distributions, and hence the redshift of the second cluster.

His redshift value of  $z = .19$  agreed closely with the known spectroscopic value of  $z = .192$ , so he extended his technique to a handful of clusters of then unknown redshifts out to maximum redshift of  $z = .46$ . He then derived a very rough value of  $\Omega_0$ . Baum's technique was fairly accurate, but because of its dependence on a large  $4000\text{\AA}$  break spectral feature, it could only work on elliptical galaxies.

## 2.2 Koo

Koo (1985) followed a different approach. First, he used photographic plates instead of a photometer, making it possible to measure photometric redshifts for a large number of galaxies simultaneously. Second, instead of using 9 filters he used only 4:  $U^+J^+F^+N^+$ . (According to Koo (1985),  $U^+ \simeq U$ ,  $J^+ \simeq J \sim B$ ,  $F^+ \simeq F \sim (V + R)/2$ , and  $N^+ \simeq I$ . Thus,  $U^+J^+F^+N^+$ , is similar to  $UB(VR)I$ .) Third, instead of using an empirical spectral energy distribution, he used the theoretical Bruzual (1983, among others) no-evolution models for all galaxy types.

The most important difference, however, was the way the colours were used. Instead of converting the photometric colours into a kind of low resolution spectrum, he converted the Bruzual templates into colours, and plotted lines of constant redshift and varying spectral type, known as *iso-z* lines, on a colour-colour diagram. Finding that the most normal colour-colour diagrams (e.g.  $U^+ - J^+$  versus  $J^+ - F^+$  and  $J^+ - F^+$  versus  $F^+ - N^+$ ) were degenerate in a range of redshifts, he invented what he called *colour-shape diagrams*. The *shape* measured whether the SED turned up or down at both

ends, that is, whether the spectrum was bowl shaped or humped. Another way to put it is that the colour measured the first derivative with respect to wavelength of the spectrum and the shape measured the second derivative. For colour he used either  $2U^+ - 2F^+$  or  $U^+ + J^+ - F^+ - N^+$ , both of which span a large wavelength range. For shape, he used either  $-U^+ + 2J^+ - F^+$  or  $-U^+ + J^+ + F^+ - N^+$ . Following this method to measure the redshift of a galaxy, Koo calculated the colour and the shape from the  $U^+ J^+ F^+ N^+$  magnitudes and plotted them on the colour-shape diagram. The redshift of the galaxy was then found by finding the *iso-z* line closest to the point representing the galaxy. Koo tested this method on a sample of 100 galaxies with known spectroscopic redshifts ranging from  $z = .025$  to  $z = .700$ .

## 2.3 Loh and Spillar

The technique of Loh and Spillar (1986b) more closely resembles that of Baum (1962) than that of Koo (1985). They collected their photometry through 6 non-standard filters, using a CCD (Charge Coupled Device) detector. The photometry was converted into low resolution spectral energy distributions. These SED's were compared with fiducial spectra for E, Sbc and Im galaxies compiled from various sources and redshifted. The redshift of the fiducial spectrum which best matched (in terms of  $\chi^2$ ) the observed SED of a galaxy gave the redshift of that galaxy. The error bars associated with each photometric redshift were found by varying the redshift of the templates until  $\chi^2$  increased by one. Loh and Spillar observed 34 galaxies of known redshift in the galaxy cluster 0023+1654 to test their method. The

standard deviation of the redshift differences ( $z_{spec} - z_{phot}$ ) was .12. Loh and Spillar went on to use their technique to measure photometric redshifts for 1000 field galaxies in order to determine a value for the density parameter of  $\Omega_0 = 0.9_{-.5}^{+.7}$  (Loh and Spillar, 1986a).

# Chapter 3

## Data

In order to design and test a method for calculating photometric redshifts, one needs multi-colour photometry and spectroscopic redshifts for a number of galaxies. Although quite a few spectroscopic redshift surveys have been published, as well as numerous photometric number-count surveys, there are very few sets of galaxies for which multi-colour photometry and spectroscopic redshift data are available. Since photometry takes far less effort than spectroscopy, (indeed, that is a major incentive for doing photometric redshifts in the first place) photometry was performed on galaxies whose spectroscopic redshifts had already been determined.

### 3.1 Observations

In January 1992, multi-colour imaging was obtained at the Canada France Hawaii Telescope of five fields containing galaxies whose redshifts had been spectroscopically determined by Colless *et al.* (1990; 1993) and Boyle, Jones & Shanks (1991). The Lick 2 2048×2048 CCD was used in the FOCAM

(Prime Focus) configuration. Exposure times were 5 minutes in each of the *VRI* bandpasses and typically 10 minutes in the *B* bandpass because of the reduced quantum efficiency of the Lick 2 chip at shorter wavelengths. For the same reason, no observations were made in the *U* bandpass. The plate scale of the prime focus at CFHT is  $13''.7/\text{mm}$ . The pixels of the Lick 2 chip are 15 microns across giving a scale of  $\sim 21''/\text{pixel}$ . The chip measures 2048 pixels by 2048 pixels, and thus the fields covered a 7 arcminute by 7 arcminute area of the sky. The field centres (in epoch 1950.0 coordinates), the exposure times for each filter and the seeing (which ranged from superb to mediocre to poor) are listed in Table 3.1.

Fields f2 and f3 were not observed because there was insufficient telescope time. Field f1 was not observed in *B* and *R* for the same reason. Standard stars in NGC 7790 and NGC 4147 were observed.

## 3.2 Image Reductions

At intervals during the run, bias frames and dome flats were recorded. The images were de-biassed and flat fielded in the usual way using IRAF (Image Reduction and Analysis Facility). The bias frames and the flat field frames were checked for any problems. Bias frames taken on different nights were subtracted one from the other and the difference frame examined. No significant deviations were found. Dividing flat fields taken on different nights by each other (flat fielding the flat fields) revealed some minor inconsistencies at the 2% level. Since the signal-to-noise ratio (SNR) of the brightest galaxies measured was typically 20 (corresponding to 5% photometry), and most

Table 3.1: List of observations

field	filter	field centers(1950.0)		night observed	exposure time	seeing
		R.A.	Dec.			
f1	<i>V</i>	13 <sup>h</sup> 41 <sup>m</sup> 12 <sup>s</sup>	-00°01'00''	11/12 Jan	300s	0''8
f1	<i>I</i>			11/12 Jan	300s	0''8
f4	<i>B</i>	10 <sup>h</sup> 43 <sup>m</sup> 56 <sup>s</sup>	+00°08'00''	8/9 Jan	600s	1''1
f4	<i>V</i>			8/9 Jan	300s	0''6
f4	<i>R</i>			8/9 Jan	300s	0''8
f4	<i>I</i>			9/10 Jan	300s	1''3
f5	<i>B</i>	10 <sup>h</sup> 43 <sup>m</sup> 56 <sup>s</sup>	-00°01'00''	10/11 Jan	600s	1''5
f5	<i>V</i>			10/11 Jan	300s	1''3
f5	<i>R</i>			10/11 Jan	300s	2''1
f5	<i>I</i>			10/11 Jan	300s	1''4
f6	<i>B</i>	10 <sup>h</sup> 43 <sup>m</sup> 52 <sup>s</sup>	-00°04'00''	11/12 Jan	600s	0''8
f6	<i>V</i>			11/12 Jan	300s	0''7
f6	<i>R</i>			11/12 Jan	300s	1''1
f6	<i>I</i>			11/12 Jan	300s	0''7
f7	<i>B</i>	00 <sup>h</sup> 54 <sup>m</sup> 53 <sup>s</sup>	-27°42'30''	8/9 Jan	300s	2''0
f7	<i>V</i>			8/9 Jan	300s	0''7
f7	<i>R</i>			8/9 Jan	300s	1''1
f7	<i>I</i>			8/9 Jan	300s	0''7

galaxies had a SNR of 10 (10% photometry) this is of little concern.

Cosmic ray hits were harder to remove than usual because only one frame was taken of each area of the sky in each band pass, meaning that median filtering was not an option. The cosmic rays were identified as being those pixels whose flux was greater than sky background by 3 times the standard deviation of the sky and whose flux ratio (the ratio between the flux of pixel in question and the average of the 8 pixels surrounding it) was greater than 10. This algorithm was run three times on each frame to get rid of multiple hits.

The frames were then scrutinized by eye for “grazing hits” where a cosmic ray strikes the chip at an oblique angle, contaminating many adjacent pixels. Such events are easily seen by eye and but are harder to detect using the algorithm above. All cosmic ray pixel values were then replaced with the average of nearby pixels that weren’t cosmic ray pixels.

Since finding charts for the Colless *et al.* (1990; 1993) galaxies were not available, they were found by offsetting from stars in the Guide Star Catalog. This procedure was relatively straightforward except that some guide “stars” are in fact galaxies. The scale of the frames was found to be  $0''.2055 \pm 0''.0009$  /pixel.

Tables 3.2 and 3.3 show the coordinates and redshifts of the galaxies whose *BVRI* magnitudes were measured. The first column gives the reference either to “Col90” (Colless et al., 1990), “Col93” (Colless et al., 1993) or “BJS91” (Boyle et al., 1991). The last column identifies the galaxies by field and number. This notation is used throughout this thesis. Fields f5 and f6 overlap. Galaxies found in both fields are labeled “fB”.

### 3.3 Photometry

Aperture photometry was used to measure the *BVRI* magnitudes of the galaxies. The exact size of the aperture was chosen with an eye to both consistency and signal-to-noise ratios. If the aperture is too small, it will sample only the core of the galaxy. This is undesirable for two reasons. Different galaxies have different brightness radial profiles which cause a different fraction of the total light from the galaxies to be included in a small aperture.

Table 3.2: The Colless galaxies: Part 1

Ref.	ID #	coordinates (1950.0)		$z$	Field and ID #
		R.A.	Dec.		
Col90	13.4.13	13 <sup>h</sup> 41 <sup>m</sup> 16 <sup>s</sup> 57	-00°03'22"9	0.419	f1.01
Col90	13.4.21	13 <sup>h</sup> 41 <sup>m</sup> 19 <sup>s</sup> 74	-00°01'33"0	0.165	f1.02
Col90	13.4.14	13 <sup>h</sup> 41 <sup>m</sup> 18 <sup>s</sup> 82	-00°03'54"4	0.273	f1.03
Col90	13.4.20	13 <sup>h</sup> 41 <sup>m</sup> 16 <sup>s</sup> 34	-00°00'49"3	0.437	f1.04
Col90	13.4.15	13 <sup>h</sup> 41 <sup>m</sup> 09 <sup>s</sup> 10	+00°00'11"7	0.415	f1.05
Col90	13.4.16	13 <sup>h</sup> 41 <sup>m</sup> 13 <sup>s</sup> 68	+00°00'31"2	0.120	f1.06
Col90	13.4.22	13 <sup>h</sup> 41 <sup>m</sup> 15 <sup>s</sup> 73	+00°00'51"9	0.086	f1.07
Col90	13.4.10	13 <sup>h</sup> 41 <sup>m</sup> 05 <sup>s</sup> 01	+00°01'14"8	0.361	f1.08
Col90	13.4.12	13 <sup>h</sup> 41 <sup>m</sup> 13 <sup>s</sup> 65	+00°02'21"5	0.120	f1.09
Col90	13.4.02	13 <sup>h</sup> 41 <sup>m</sup> 06 <sup>s</sup> 05	-00°02'50"8	0.127	f1.10
Col90	10.4.17	10 <sup>h</sup> 43 <sup>m</sup> 57 <sup>s</sup> 45	-00°01'59"8	0.191	fB.11
Col90	10.2.17	10 <sup>h</sup> 44 <sup>m</sup> 04 <sup>s</sup> 53	+00°00'18"3	0.302	f5.12
Col90	10.2.05	10 <sup>h</sup> 44 <sup>m</sup> 02 <sup>s</sup> 86	+00°00'58"5	0.303	f5.13
Col90	10.2.14	10 <sup>h</sup> 43 <sup>m</sup> 59 <sup>s</sup> 00	-00°00'05"7	0.304	f5.14
Col90	10.2.23	10 <sup>h</sup> 44 <sup>m</sup> 04 <sup>s</sup> 00	+00°01'53"1	0.665	f5.15
Col90	10.4.06	10 <sup>h</sup> 43 <sup>m</sup> 47 <sup>s</sup> 34	-00°02'17"8	0.237	fB.16
Col90	10.4.10	10 <sup>h</sup> 43 <sup>m</sup> 59 <sup>s</sup> 11	-00°07'34"0	0.290	f6.17
Col90	10.4.13	10 <sup>h</sup> 43 <sup>m</sup> 46 <sup>s</sup> 45	-00°06'40"5	0.148	f6.18
Col90	10.4.15	10 <sup>h</sup> 43 <sup>m</sup> 59 <sup>s</sup> 26	-00°06'19"4	0.394	f6.19
Col90	10.4.12	10 <sup>h</sup> 44 <sup>m</sup> 00 <sup>s</sup> 02	-00°04'44"4	0.437	f6.20
Col90	10.2.01	10 <sup>h</sup> 43 <sup>m</sup> 55 <sup>s</sup> 12	+00°10'04"1	0.266	f4.21
Col90	10.2.02	10 <sup>h</sup> 43 <sup>m</sup> 48 <sup>s</sup> 77	+00°07'38"6	0.549	f4.22
Col90	10.2.04	10 <sup>h</sup> 43 <sup>m</sup> 55 <sup>s</sup> 81	+00°08'50"6	0.543	f4.23
Col90	10.2.11	10 <sup>h</sup> 44 <sup>m</sup> 01 <sup>s</sup> 25	+00°09'41"5	0.277	f4.24
Col90	10.2.12	10 <sup>h</sup> 44 <sup>m</sup> 05 <sup>s</sup> 59	+00°05'20"6	0.168	f4.25
Col90	10.2.15	10 <sup>h</sup> 43 <sup>m</sup> 49 <sup>s</sup> 40	+00°08'11"9	0.451	f4.26
Col90	10.2.16	10 <sup>h</sup> 44 <sup>m</sup> 00 <sup>s</sup> 69	+00°06'17"5	0.151	f4.27

Table 3.3: The Colless galaxies: Part 2

Ref.	ID #	coordinates (1950.0)		$z$	Field and ID #
		R.A.	Dec.		
Col90	10.2.19	10 <sup>h</sup> 43 <sup>m</sup> 56 <sup>s</sup> 27	+00°05'48"9	0.179	f4.28
Col90	10.2.20	10 <sup>h</sup> 43 <sup>m</sup> 45 <sup>s</sup> 16	+00°07'16"6	0.188	f4.29
Col90	10.2.22	10 <sup>h</sup> 43 <sup>m</sup> 49 <sup>s</sup> 11	+00°11'09"3	0.180	f4.30
Col90	10.2.25	10 <sup>h</sup> 43 <sup>m</sup> 48 <sup>s</sup> 10	+00°06'38"0	0.160	f4.31
Col90	00.2.12	00 <sup>h</sup> 55 <sup>m</sup> 00 <sup>s</sup> 17	-27°40'47"9	0.113	f7.32
Col90	00.2.03	00 <sup>h</sup> 54 <sup>m</sup> 55 <sup>s</sup> 84	-27°39'54"6	0.331	f7.33
Col90	00.2.19	00 <sup>h</sup> 54 <sup>m</sup> 53 <sup>s</sup> 12	-27°41'06"7	0.217	f7.34
Col90	00.2.05	00 <sup>h</sup> 54 <sup>m</sup> 56 <sup>s</sup> 58	-27°40'31"4	0.330	f7.35
Col90	00.2.11	00 <sup>h</sup> 54 <sup>m</sup> 55 <sup>s</sup> 10	-27°39'25"2	0.421	f7.36
Col90	00.2.02	00 <sup>h</sup> 54 <sup>m</sup> 48 <sup>s</sup> 49	-27°44'50"9	0.165	f7.37
Col90	00.2.13	00 <sup>h</sup> 54 <sup>m</sup> 54 <sup>s</sup> 03	-27°41'44"6	0.317	f7.38
Col90	00.2.16	00 <sup>h</sup> 54 <sup>m</sup> 49 <sup>s</sup> 15	-27°41'55"4	0.439	f7.39
Col90	00.2.17	00 <sup>h</sup> 54 <sup>m</sup> 48 <sup>s</sup> 47	-27°39'36"5	0.329	f7.40
Col90	00.2.24	00 <sup>h</sup> 54 <sup>m</sup> 49 <sup>s</sup> 44	-27°45'40"3	0.255	f7.41
Col90	00.2.25	00 <sup>h</sup> 54 <sup>m</sup> 57 <sup>s</sup> 21	-27°43'05"0	0.317	f7.42
Col90	00.2.26	00 <sup>h</sup> 54 <sup>m</sup> 57 <sup>s</sup> 76	-27°44'09"0	0.333	f7.43
Col90	00.2.31	00 <sup>h</sup> 54 <sup>m</sup> 46 <sup>s</sup> 93	-27°40'08"1	0.464	f7.44
Col90	00.2.41	00 <sup>h</sup> 54 <sup>m</sup> 48 <sup>s</sup> 39	-27°42'32"4	0.421	f7.45
Col90	00.2.42	00 <sup>h</sup> 54 <sup>m</sup> 56 <sup>s</sup> 25	-27°44'35"7	0.563	f7.46
Col90	00.2.48	00 <sup>h</sup> 54 <sup>m</sup> 54 <sup>s</sup> 97	-27°45'52"6	0.176	f7.47
BJS91	F855:097	10 <sup>h</sup> 44 <sup>m</sup> 10 <sup>s</sup> 20	+00°01'17"0	0.120	f5.48
Col93	10.4.03	10 <sup>h</sup> 43 <sup>m</sup> 52 <sup>s</sup> 63	-00°00'59"2	0.276	fB.50
Col93	10.4.23	10 <sup>h</sup> 43 <sup>m</sup> 51 <sup>s</sup> 88	-00°01'33"4	0.441	fB.51
Col93	10.4.26	10 <sup>h</sup> 43 <sup>m</sup> 45 <sup>s</sup> 68	-00°02'35"8	0.323	fB.52
Col93	10.4.32	10 <sup>h</sup> 43 <sup>m</sup> 56 <sup>s</sup> 31	-00°04'23"3	0.439	fB.53
Col93	10.4.04	10 <sup>h</sup> 43 <sup>m</sup> 48 <sup>s</sup> 52	-00°05'56"7	0.154	f6.54

Further, the galaxies being considered here are only semi-resolved: the sizes of the cores of the galaxies are not much larger than the size of the point spread function. Thus, changes in the seeing can produce changes in the fraction of light included in an overly small aperture. Conversely, if the aperture is too big, the increased amount of sky background light tends to drown out the light from the galaxy, resulting in a low signal-to-noise ratio. Thus, the best aperture size is one big enough that repeatability of the photometry under different seeing conditions is not a problem, but no bigger.

Since fields f5 and f6 overlapped, it was possible to quantify these effects. Field f5 was observed on the night of the 10/11<sup>th</sup> of January in relatively poor seeing conditions, whereas f6 was observed the following night when the seeing was much better (see Table 3.1). The best aperture was found to be 5 arcseconds in diameter.

The sky background around each galaxy was measured in an annulus with an inner radius of 8.2 arcseconds (20 pixels) and an outer radius of 12.3 arcseconds (30 pixels).

Standard stars were observed to calibrate the photometry. Because of time constraints, only one field of standard stars was observed each night. These observations did not allow the calculation of extinction coefficients but colour terms could be derived. Standard extinction coefficients were taken from the CFHT Observers Manual (Monnet, 1990). Since the standard fields were in the same general vicinity of the sky as the galaxies being observed, the difference in airmass between the standards and the galaxies was small; hence the small possible uncertainties in the extinction coefficients will translate into much smaller uncertainties in the derived magnitudes. On all nights

and through all filters, the colour terms were found to be extremely close to zero. They were therefore ignored in all subsequent analysis. Thus the only terms that needed to be derived each night were the zero points for each filter.

No corrections were made for galactic extinction and reddening. At the relatively high galactic latitudes ( $|b| = 50^\circ$  and up) the extinction coefficients are quite small. For the  $B$  band, the extinction is  $A(B) \lesssim 0.09$ ; the coefficients are smaller for the redder filters (Burstein and Heiles, 1982). Further, only the colours are really relevant when determining photometric redshifts. The effects of reddening on the colours is less than the effects of extinction on the magnitudes:  $E(B - V) \lesssim 0.02$ .

Tables 3.4 and 3.5 show the  $BVRI$  photometry for the Colless galaxies listed in Tables 3.2 and 3.3. Galaxies f1.01 through f1.10 have no  $B$  and  $R$  magnitudes because they were not observed in those band passes. Galaxy f1.09 was located so close to the edge of the frame that aperture photometry was impossible. The galaxy designated as # 10.4.12 in Colless *et al.* (1990), when resolved in the superb seeing conditions on Mauna Kea, turned out to be a close pair of galaxies. They have been treated separately as f6.20a and f6.20b in this thesis. It was assumed that they both were at the same redshift,  $z = .437$ .

All the galaxies from Tables 3.4 and 3.5 that had photometric data in all four filters ( $BVRI$ ) and did not lie on bad columns of the CCD frames were included in Tables 3.6 and 3.7. From this table of spectroscopic redshifts and photometry a technique for determining photometric redshifts was developed.

Table 3.4: Photometry for the Colless galaxies: Part 1

ID #	$B$	$\Delta B$	$V$	$\Delta V$	$R$	$\Delta R$	$I$	$\Delta I$
f1.01	–	–	20.789	0.054	–	–	19.312	0.036
f1.02	–	–	21.562	0.105	–	–	20.547	0.106
f1.03	–	–	20.953	0.061	–	–	19.375	0.037
f1.04	–	–	21.294	0.081	–	–	19.886	0.059
f1.05	–	–	20.565	0.045	–	–	18.511	0.018
f1.06	–	–	21.177	0.076	–	–	20.355	0.092
f1.07	–	–	21.657	0.113	–	–	21.208	0.197
f1.08	–	–	20.645	0.046	–	–	19.558	0.045
f1.09	–	–	–	–	–	–	–	–
f1.10	–	–	21.044	0.066	–	–	20.304	0.085
fB.11	21.864	0.069	21.077	0.055	20.554	0.036	20.050	0.053
f5.12	22.170	0.128	21.013	0.066	20.569	0.046	20.087	0.071
f5.13	21.763	0.092	20.459	0.420	19.747	0.022	19.023	0.027
f5.14	21.980	0.110	20.626	0.470	19.951	0.027	19.276	0.034
f5.15	22.419	0.160	22.013	0.157	21.923	0.145	20.897	0.146
fB.16	22.283	0.094	21.206	0.058	20.199	0.029	18.579	0.026
f6.17	21.206	0.058	20.333	0.045	19.702	0.028	19.153	0.041
f6.18	22.679	0.184	21.593	0.102	20.869	0.056	19.851	0.060
f6.19	22.000	0.104	20.837	0.060	20.181	0.036	19.416	0.045
f6.20a	21.527	0.070	20.893	0.060	20.169	0.036	20.294	0.082
f6.20b	22.334	0.138	20.902	0.062	19.558	0.027	18.716	0.034
f4.21	21.486	0.072	20.693	0.054	20.140	0.056	19.628	0.062
f4.22	21.575	0.076	20.936	0.065	20.659	0.086	20.443	0.127
f4.23	21.650	0.085	21.361	0.096	20.668	0.090	20.743	0.169
f4.24	21.485	0.074	20.435	0.045	20.016	0.050	19.475	0.055
f4.25	21.687	0.085	20.384	0.043	19.585	0.036	18.923	0.035
f4.26	21.927	0.100	21.111	0.075	20.217	0.058	19.487	0.054
f4.27	22.351	0.147	21.268	0.087	21.207	0.138	20.439	0.126

Table 3.5: Photometry for the Colless galaxies: Part 2

ID #	$B$	$\Delta B$	$V$	$\Delta V$	$R$	$\Delta R$	$I$	$\Delta I$
f4.28	22.090	0.119	21.147	0.079	20.826	0.099	20.220	0.106
f4.29	21.963	0.106	21.506	0.107	20.647	0.089	19.576	0.064
f4.30	22.698	0.196	21.386	0.096	21.559	0.204	21.287	0.280
f4.31	22.580	0.177	22.149	0.187	21.266	0.147	20.604	0.147
f7.32	21.473	0.141	21.146	0.098	20.712	0.067	20.284	0.094
f7.33	21.584	0.146	20.250	0.046	19.482	0.028	18.718	0.027
f7.34	24.330	1.805	21.940	0.196	21.632	0.159	20.940	0.164
f7.35	–	–	21.690	0.161	20.874	0.086	20.720	0.140
f7.36	21.913	0.206	20.380	0.053	19.359	0.025	18.557	0.024
f7.37	21.809	0.186	20.692	0.070	20.335	0.053	19.635	0.053
f7.38	21.983	0.217	20.496	0.057	19.483	0.028	18.672	0.025
f7.39	22.991	0.551	21.137	0.094	20.507	0.060	19.761	0.059
f7.40	22.552	0.358	20.635	0.061	19.717	0.033	18.716	0.027
f7.41	22.348	0.303	21.877	0.184	21.611	0.149	21.046	0.182
f7.42	23.878	1.196	21.410	0.125	21.009	0.088	20.664	0.131
f7.43	23.096	0.589	21.241	0.102	20.869	0.078	20.056	0.073
f7.44	22.254	0.266	21.650	0.155	20.897	0.083	20.423	0.105
f7.45	23.691	0.998	21.384	0.119	20.215	0.047	19.315	0.041
f7.46	22.619	0.392	22.337	0.292	21.445	0.146	20.629	0.137
f7.47	23.048	0.561	22.603	0.369	22.173	0.288	–	–
f5.48	20.492	0.035	19.592	0.024	19.135	0.015	18.664	0.022
fB.50	21.728	0.083	21.171	0.078	20.887	0.062	20.493	0.094
fB.51	23.025	0.265	21.294	0.087	20.034	0.033	19.188	0.040
fB.52	21.638	0.070	20.872	0.060	20.247	0.035	20.206	0.082
fB.53	22.304	0.101	20.820	0.059	19.909	0.031	19.168	0.040
f6.54	21.570	0.075	21.192	0.073	20.974	0.061	20.446	0.093

Table 3.6: The galaxies used for developing the photometric redshift technique: Part 1

ID #	$z$	$B$	$V$	$R$	$I$
fB.11	0.191	21.864	21.077	20.554	20.050
f5.12	0.302	22.170	21.013	20.569	20.087
f5.13	0.303	21.763	20.459	19.747	19.023
f5.14	0.304	21.980	20.626	19.951	19.276
f5.15	0.665	22.419	22.013	21.923	20.897
f6.17	0.290	21.206	20.333	19.702	19.153
f6.19	0.394	22.000	20.837	20.181	19.416
f6.20a	0.437	21.527	20.893	20.169	20.294
f6.20b	0.437	22.334	20.902	19.558	18.716
f4.21	0.266	21.486	20.693	20.140	19.628
f4.22	0.549	21.575	20.936	20.659	20.443
f4.23	0.543	21.650	21.361	20.668	20.743
f4.24	0.277	21.485	20.435	20.016	19.475
f4.25	0.168	21.687	20.384	19.585	18.923
f4.27	0.151	22.351	21.268	21.207	20.439
f4.28	0.179	22.090	21.147	20.826	20.220
f4.30	0.180	22.698	21.386	21.559	21.287
f4.31	0.160	22.580	22.149	21.266	20.604
f7.32	0.113	21.473	21.146	20.712	20.284
f7.33	0.331	21.584	20.250	19.482	18.718
f7.34	0.217	24.330	21.940	21.632	20.940
f7.36	0.421	21.913	20.380	19.359	18.557
f7.37	0.165	21.809	20.692	20.335	19.635
f7.38	0.317	21.983	20.496	19.483	18.672
f7.39	0.439	22.991	21.137	20.507	19.761
f7.40	0.329	22.552	20.635	19.717	18.716
f7.41	0.255	22.348	21.877	21.611	21.046
f7.42	0.317	23.878	21.410	21.009	20.664
f7.43	0.333	23.096	21.241	20.869	20.056
f7.44	0.464	22.254	21.650	20.897	20.423

Table 3.7: The galaxies used for developing the photometric redshift technique: Part 2

ID #	$z$	$B$	$V$	$R$	$I$
f7.45	0.421	23.691	21.384	20.215	19.315
f7.46	0.563	22.619	22.337	21.445	20.629
f5.48	0.120	20.492	19.592	19.135	18.664
fB.50	0.276	21.728	21.171	20.887	20.493
fB.51	0.441	23.025	21.294	20.034	19.188
fB.52	0.323	21.638	20.872	20.247	20.206
fB.53	0.439	22.304	20.820	19.909	19.168
f6.54	0.154	21.570	21.192	20.974	20.446

# Chapter 4

## Basic technique

This chapter describes in detail the photometric redshift technique presented in this thesis. It can be divided into three steps:

First, the photometric data for each galaxy in the fields were converted into spectral energy distributions (SED's). The magnitude in each bandpass was converted to a flux in units of  $\text{W } \mu\text{m}^{-1} \text{ cm}^{-2}$  at the central or effective wavelength,  $\lambda_{cen}$ , of the bandpass. When the flux was plotted against wavelength for each of the *BVRI* bandpasses, the equivalent of a low dispersion (spectral coverage from 4000 to 9000 Å), low resolution (sampled at only 4 wavelengths) spectrum was created.

Second, a collection of template spectra of all Hubble types and redshifts ranging from  $z = 0$  to  $z = 1$  was compiled. In order to compare on an equal basis the template spectra and the observed low resolution spectral energy distributions, the continuous spectra were reduced to fluxes at the four wavelengths corresponding to the *BVRI* filters.

Third, the spectral energy distribution derived from the observed *BVRI* magnitudes of each object was compared to each template spectrum in turn.

The best matching spectrum and hence the redshift was determined by minimizing  $\chi^2$ .

In the following sections, each of these steps is examined in turn.

## 4.1 Photometry to spectral energy distributions

The first step was to convert the photometric data (measured in terms of magnitudes) to spectral energy distributions (measured in terms of flux). It is said that anyone who makes a significant contribution to any field of endeavour becomes an obstruction to its progress in direct proportion to the importance of his or her original contribution. If this is true of anybody, it is true of Hipparchus who developed the magnitude system which has been alternately a boon and a plague to astronomers for the last 2000 years. Although the magnitude system is convenient in many instances, it has one major deficiency. It is not directly obvious what the shape of the spectral energy distribution of a source is by looking at its magnitudes and colours.

Luminosity,  $L$ , is related to absolute magnitude,  $M$ , by

$$M = -2.5 \log(L/L_0), \quad (4.1)$$

where  $L_0$  is the luminosity zero-point. If a source's luminosity is  $L_0$ , then its magnitude is  $M = 0$ . For a given unit wavelength and unit surface area, equation 4.1 becomes

$$M = -2.5 \log(F/F_0), \quad (4.2)$$

where  $F$  is the flux in units of  $\text{W } \mu\text{m}^{-1} \text{ cm}^{-2}$  and  $F_0$  is the flux zero-point. The *BVRI* magnitude systems are calibrated to the type A0 star, Vega, which

has  $B = V = R = I = 0$  by definition. By using information from Monnet (1990), Illingworth (1985) and Johnson (1966), it was possible to derive the flux zero-points for the *BVRI* filters. This information is summarized in Table 4.1.

Table 4.1: Filter properties

Filter	$\lambda_{cen}$	$\Delta\lambda$	$F_0$
B	4300 Å	1000 Å	$6.61 \times 10^{-12} \text{ W}/\mu\text{m}/\text{cm}^2$
V	5420 Å	900 Å	$3.77 \times 10^{-12} \text{ W}/\mu\text{m}/\text{cm}^2$
R	6480 Å	1270 Å	$2.18 \times 10^{-12} \text{ W}/\mu\text{m}/\text{cm}^2$
I	8310 Å	1970 Å	$1.08 \times 10^{-12} \text{ W}/\mu\text{m}/\text{cm}^2$

To convert *BVRI* magnitudes into a spectral energy distribution one inverts equation 4.2,

$$F = F_0 10^{-M/2.5}, \quad (4.3)$$

for each of the bandpasses and plots the resulting fluxes against the central wavelength of each filter. For small values, absolute uncertainties in the magnitudes are roughly equivalent to relative uncertainties in the fluxes:

$$\begin{aligned}
 \Delta M &= M_1 - M_2 \\
 &= 2.5 \log(F_2/F_1), \text{ if } \Delta F = F_2 - F_1 \\
 &= 2.5 \log\left(1 + \frac{\Delta F}{F_1}\right) \\
 &\simeq \frac{2.5}{\ln 10} \frac{\Delta F}{F_1} \\
 \Delta M &\simeq \frac{\Delta F}{F}
 \end{aligned} \quad (4.4)$$

Figure 4.1 shows an example of the process. Here, the galaxy f6.20b from Table 3.6 ( $B = 22.334, V = 20.902, R = 19.558, I = 18.716$ ) has been converted into a SED.

## 4.2 The template spectra

The template spectra were derived from the spectra published by Bruzual (1985): the spectrum of an average elliptical galaxy (Hubble type E) and that of an irregular galaxy (type Sm/Irr). Other sources could have been used for the spectra (e.g. Pence (1976)). However, there is very little difference between the spectra in the various different sources. Very few sources in the literature give the extended coverage in the ultra-violet region that is necessary when spectra are to be redshifted. Figure 4.2 shows the two spectra. The irregular galaxy has had its emission lines removed.

A note on terminology is perhaps in order here. Within this thesis, words such as “morphology”, “Hubble type”, “Sb galaxies”, and “early/late types”, are used to describe the spectral properties of galaxies even though, properly speaking, they refer only to the physical appearance of galaxies on the sky. “Spectral Hubble type” and Hubble type are not necessarily the same; the spectral Hubble type reflects the stellar population of a galaxy rather than its structure. However, the appearances and spectra of galaxies are correlated: the spectra of different elliptical galaxies are quite similar, the spectra of different examples of the same Hubble type spiral galaxies are consistent and so on. It is therefore convenient to describe the spectra in terms of their visual counterparts.

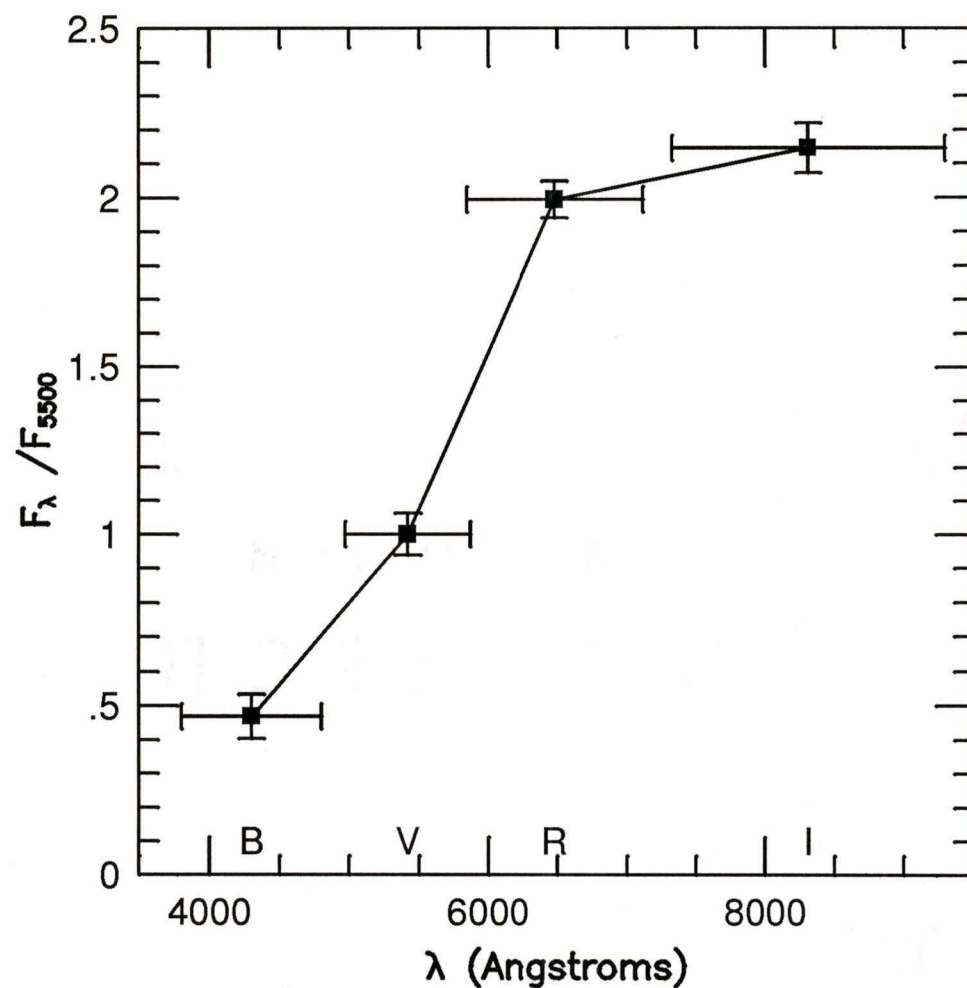


Figure 4.1: The *BVRI* photometry of galaxy f6.20b converted into a spectral energy distribution. The horizontal error bars show the width of each passband. The vertical error bars indicate photometric errors.

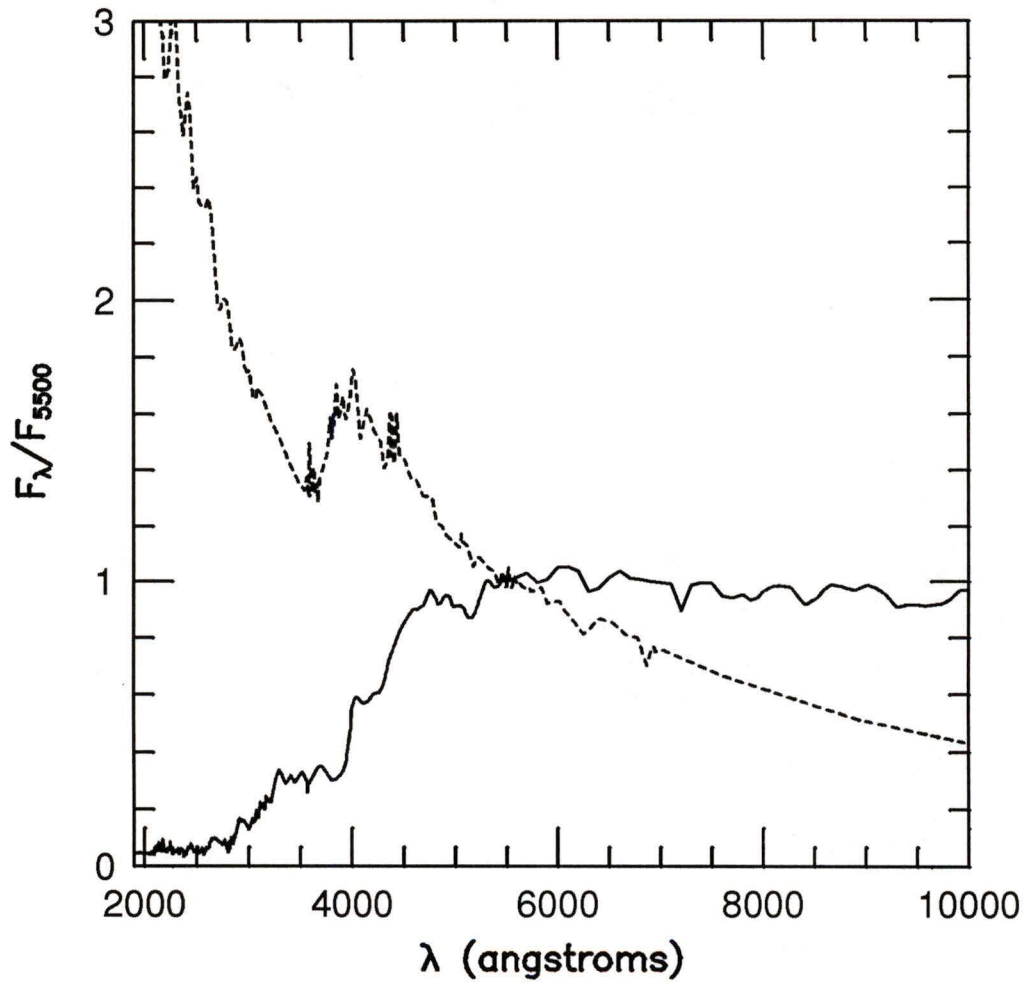


Figure 4.2: The spectra of elliptical (solid line) and irregular (dashed line) galaxies from Bruzual (1985).

All types of galaxies can be thought of as containing a bulge component and a disk component. The bulge contains old, red stars with little or no star formation. The disk contains younger, bluer stars which are constantly renewed. Ellipticals are pure bulge and irregulars are pure disk; spiral galaxies contain both components in varying ratios. Thus, to construct spectra for all types of galaxies, one need only mix the spectra of an elliptical and an irregular galaxy. Connolly *et al.* (1994), using principal component analysis, found that the spectra of all types of galaxies could be produced to within 1% using only two eigenspectra: an “average spectrum” and a “deviation spectrum”. This approach was tried but found to be equivalent to mixing complementary amounts of elliptical and irregular spectra.

Let  $m$  denote the *spectral morphology* of a galaxy in the following way:  $m = f_e$  where  $f_e$  is the fraction of light coming from the bulge of a galaxy. If  $f_s$  is the fraction of light coming the disk of a galaxy, then  $f_e + f_s = 1$ . For an elliptical ( $m = 1$ ),  $f_e = 1$  and  $f_s = 0$ . For an irregular ( $m = 0$ ),  $f_e = 0$  and  $f_s = 1$ . For a spiral galaxy ( $m = 0.4$ , let's say), the fraction of light coming from the bulge would be  $f_e = 0.4$  and so  $f_s = 0.6$ . Table 4.2 shows the values of  $m$ ,  $f_e$  and  $f_s$  for various spectral Hubble types.

Figure 4.3 shows the spectrum (dotted line) of the Sb galaxy NGC 3627 from Kennicutt (1992). On the same figure is the spectrum generated by adding together  $f_e = 0.7$  of the elliptical and  $f_s = 0.3$  of the irregular spectra from Figure 4.2 (solid line). The good match between the synthesized spectrum and the observed spectrum lends credence to the hypothesis that all galaxy spectra can be generated by a combination of just two spectra. Similar figures have been generated for Hubble types E/S0, Sa, Sb, Sc and

Table 4.2: Spectral morphologies

Type	$m$	$f_e$	$f_s$
E/S0	1.0	1.0	0.0
Sa	0.9	0.9	0.1
Sb	0.7	0.7	0.3
Sc	0.4	0.4	0.6
Irr	0.0	0.0	1.0

Irr. All types show a good match except for the absence of emission lines in the later type spectra. Although the emission lines ([OII] 3727Å and other star formation lines) can be eye-catching features of a spectrum, they contribute very little ( $\sim 2\%$ ) to the average flux over the width of a broad band filter.

It is relatively straightforward to redshift a spectrum. If the spectrum is stored in two columns, wavelength and flux at that wavelength, one has but to multiply each wavelength by  $(1 + z)$ , where  $z$  is the desired redshift, and renormalize the spectrum's flux. Figure 4.4 shows an example of this process. An elliptical galaxy has been redshifted from  $z = 0$  to  $z = .3$  and renormalized so that the flux at 5500Å is unity.

In order to compare the template spectra with the SED's of the observed galaxies, the redshifted spectra were reduced to the fluxes at the central wavelengths of the 4 passbands.

This can be done in one of two ways. The simplest is to approximate the response function of the passband with a "boxcar" function: one that is 1 within the wavelength range of the filter and 0 elsewhere. This is equivalent

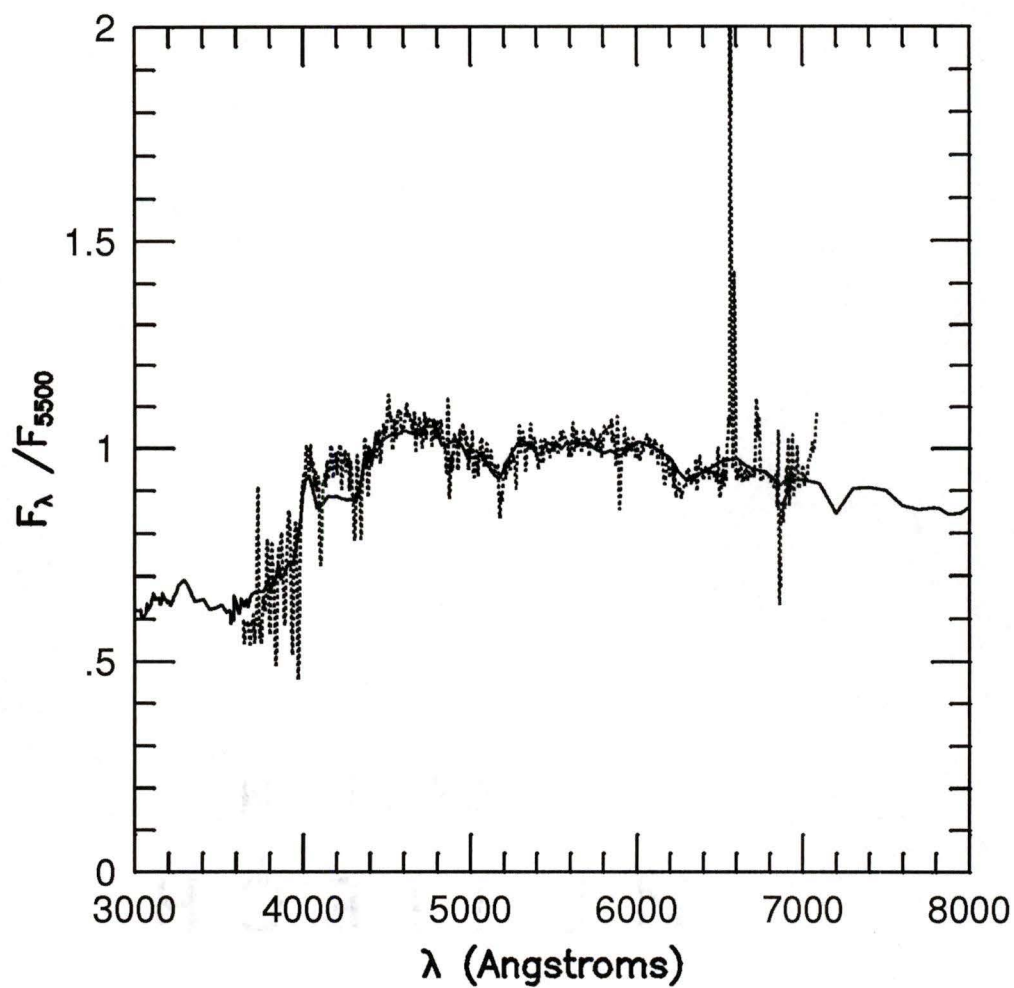


Figure 4.3: The spectrum of an Sb galaxy constructed from the two spectra in Figure 4.2 (solid line) and the spectrum of the Sb galaxy NGC 3627 (dotted line) from Kennicutt (1992).

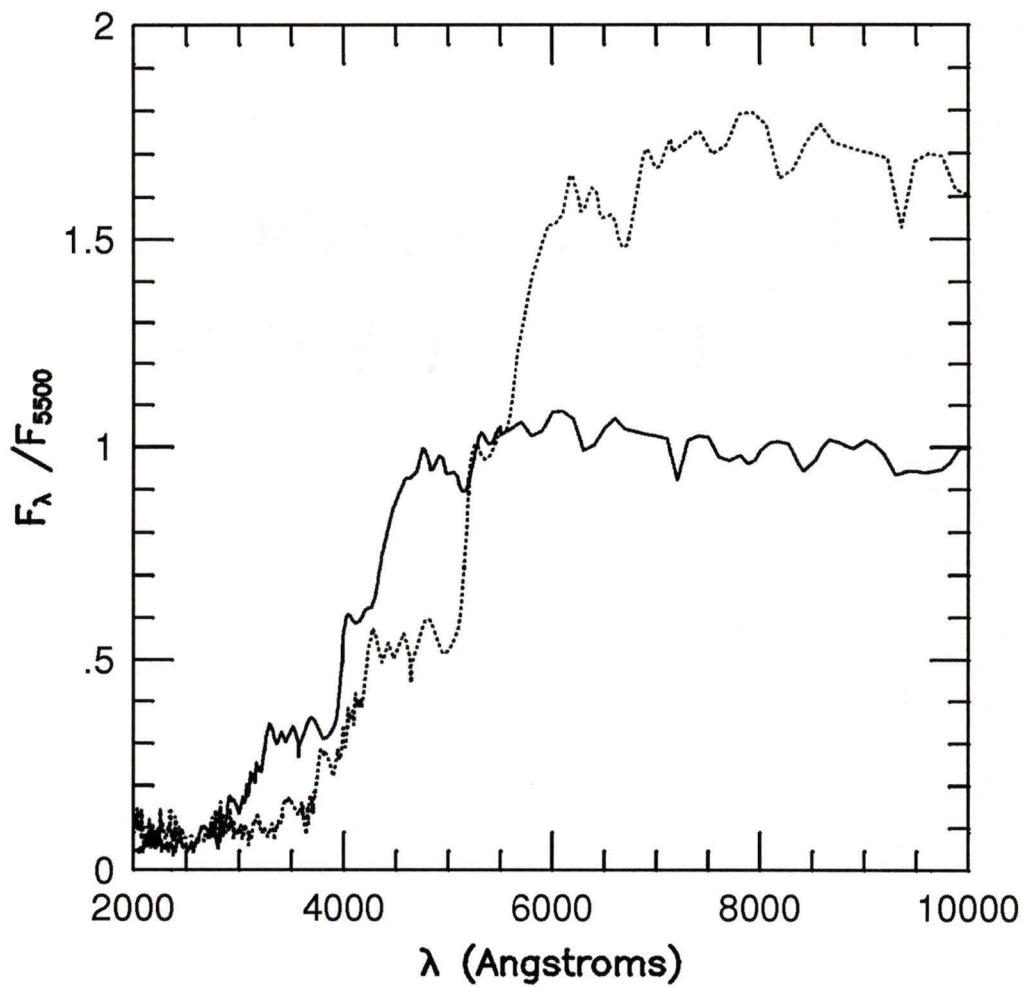


Figure 4.4: The spectrum of an E/S0 galaxy at  $z = 0$  (solid line) and redshifted to  $z = .3$  (dotted line) and renormalized.

to integrating the flux of the template over the width of the passband and then dividing by the width of the passband. In other words,

$$F_{pb} = \frac{\int_{\lambda_1}^{\lambda_2} T(\lambda) d\lambda}{\lambda_2 - \lambda_1}, \quad (4.5)$$

where  $F_{pb}$  is the flux in the passband,  $\lambda_1$  and  $\lambda_2$  are the upper and lower limits the passband, and  $T(\lambda)$  is the flux of the template spectra as a function of wavelength. One can also take the exact response function of the passband  $P(\lambda)$  into account. Then:

$$F_{pb} = \frac{\int_{\lambda_1}^{\lambda_2} T(\lambda) P(\lambda) d\lambda}{\int_{\lambda_1}^{\lambda_2} P(\lambda) d\lambda}, \quad (4.6)$$

where  $\lambda_1$  and  $\lambda_2$  now represent the wavelengths where the passband response function falls to zero. Because the template spectra vary relatively smoothly, the two methods are approximately equivalent. Figure 4.5 shows an example of this process. Here, the spectrum of E/S0 galaxy at  $z = .3$  has been reduced to the average fluxes at central wavelengths of the *BVRI* passbands.

The above process — interpolating the morphology, redshifting the resulting spectra, and reducing them to four fluxes — was performed for a wide range of morphologies and redshifts. The morphology was varied from  $m = 0$  to  $m = 1$  in steps of  $\Delta m = .01$  and the redshifts ranged from  $z = 0$  to  $z = 1$  in steps of  $\Delta z = .01$  for a total of 10 201 combinations.

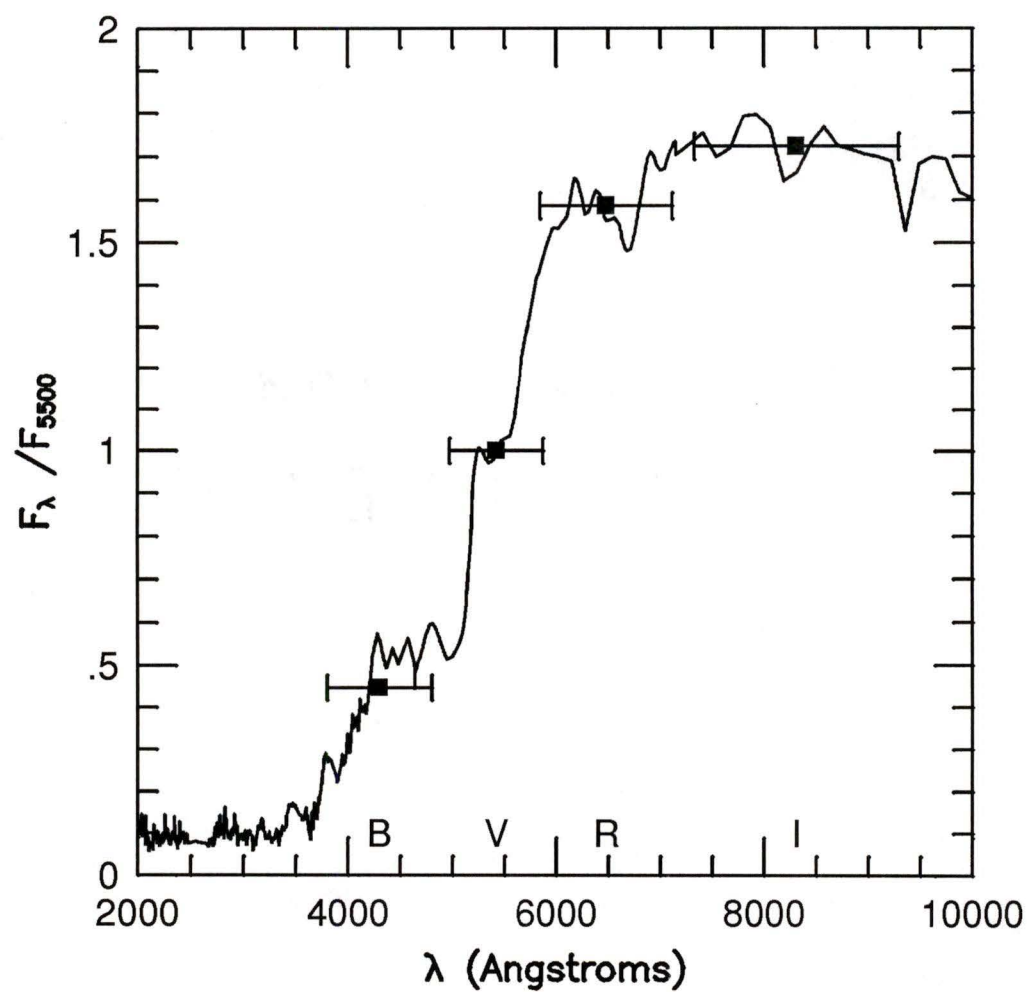


Figure 4.5: The spectrum of an E/S0 galaxy at  $z = .3$  (solid line) reduced to its fluxes at the central wavelengths of the *BVRI* passbands (points). The horizontal error bars represent the width of each passband.

### 4.3 Comparing the templates to the SED's

Given a spectral energy distribution of a galaxy of unknown redshift and a set of templates, the next step is to compare the SED to each of the templates in turn and to the template which most closely matches the SED. The degree to which each template matches the observed SED is quantified in the following manner:

$$\chi^2(m, z) = \sum_{i=BVRI} \frac{(F_i - \alpha T_i(m, z))^2}{\Delta F_i^2}, \quad (4.7)$$

where  $F_i$  and  $\Delta F_i$  are the flux and the uncertainty in the flux in each bandpass of the observed galaxy,  $T_i$  is the flux in each bandpass of the template being considered, and  $\alpha$  is a normalization factor. A normalization factor is necessary to compare properly the galaxies and the templates because the fluxes of the galaxies are very small relative to the fluxes of the templates ( $V = 20$  is  $10^8$  times fainter than  $V = 0$ ). For fixed values of  $m$  and  $z$ ,  $\chi^2$  can be minimized with respect to  $\alpha$ . By setting the derivative of equation 4.7 with respect to  $\alpha$  equal to zero, a closed formula for  $\alpha$  can be found:

$$\alpha = \frac{\sum_{i=BVRI} F_i T_i}{\sum_{i=BVRI} F_i^2}. \quad (4.8)$$

Each template is compared in turn to the target galaxy SED and the smallest value of  $\chi^2$  is found. The best matching template gives  $z_{phot}$ , the sought-after photometric redshift of the galaxy, and  $m$ , the morphology, as a bonus.

Figure 4.6 shows an example of a comparison: galaxy f7.40, whose spectroscopic redshift is  $z = 0.329$ , has been identified as an elliptical galaxy ( $m = 1.00$ ) at redshift  $z = 0.30$ . Another example is shown in Figure 4.7.

This time the galaxy f7.44 ( $z = 0.464$ ) is identified as Sc galaxy ( $m = 0.37$ ) at redshift  $z = 0.45$ .

## 4.4 Results

The technique described above was applied to the galaxies in Tables 3.6 and 3.7. Tables 4.3 and 4.4 list the resulting photometrically determined morphologies and redshifts and compare them with the spectroscopic redshifts. The differences between the spectroscopic and photometric redshifts,  $\Delta z$ , have an average of  $\langle \Delta z \rangle = 0.052$  and a standard deviation of  $\sigma(\Delta z) = .127$ , which is comparable to the results of others, e.g., Loh and Spillar (1986b).

However, as Figure 4.8 shows,  $\Delta z$  shows a distinct and undesirable trend when plotted against spectroscopic redshift. A least-squares fit shows that the slope is  $b = 0.54$ . This trend is seen in Figures 7a and 7b of Koo (1985) and in the data of Loh and Spillar (1986b). The source of this trend has been exhaustively researched. It is most likely due to a combination of two factors: a bias in the technique and evolution.

Because the photometric redshift technique described above does not allow for redshifts less than  $z = 0$  or greater than  $z = 1$ , the otherwise Gaussianly distributed points must lie between the solid lines of Figure 4.8. This will change the shape of the distribution. Particularly at the low-redshift end of Figure 4.8, some galaxies that might, through the vagaries of Gaussian error distribution, have had a negative photometric redshift were redistributed to some positive redshift. This redistribution will cause a shift to a smaller redshift difference because  $\Delta z = z_{spec} - z_{phot}$ .

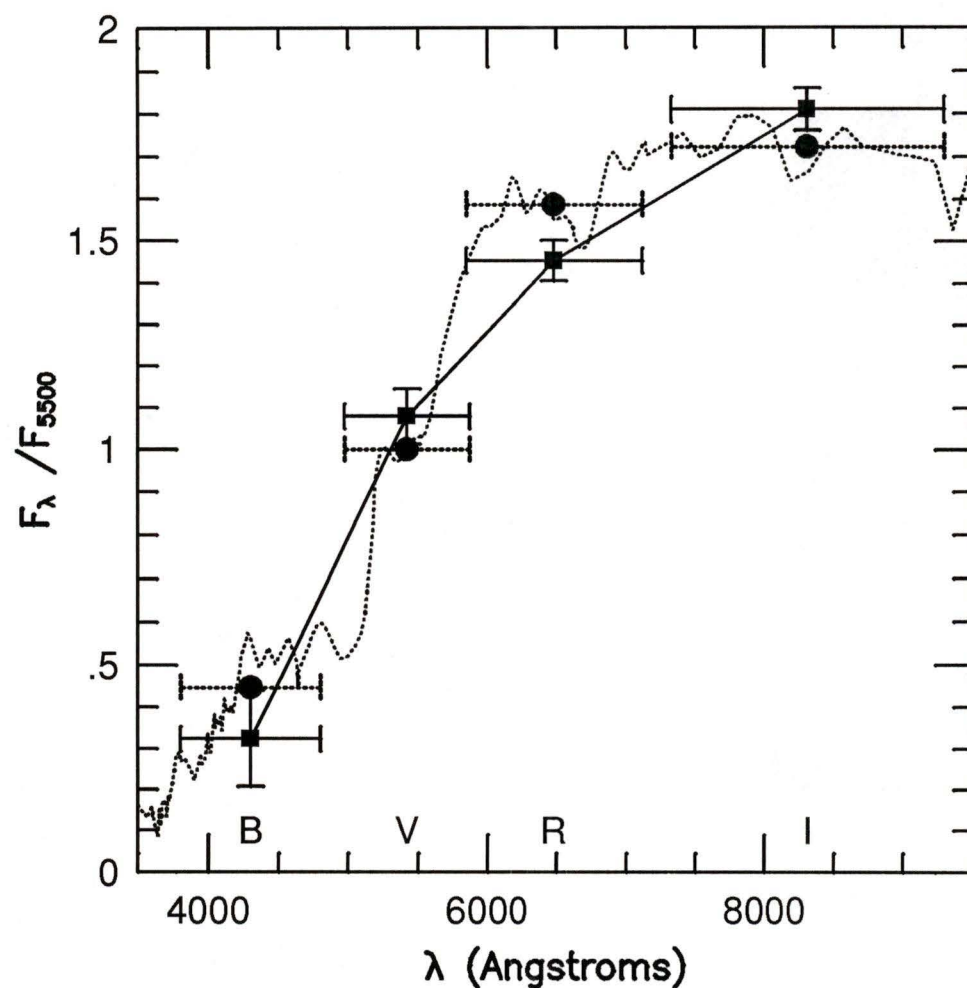


Figure 4.6: The SED of a galaxy whose spectroscopic redshift is  $z = 0.329$  (solid line and squares), identified as an elliptical galaxy ( $m = 1.00$ ) at redshift  $z = 0.30$  (dotted lines and circles). The solid vertical error bars indicate photometric errors. The dotted line shows the template spectrum and circles show it reduced to four fluxes. The horizontal error bars show the width of each passband.

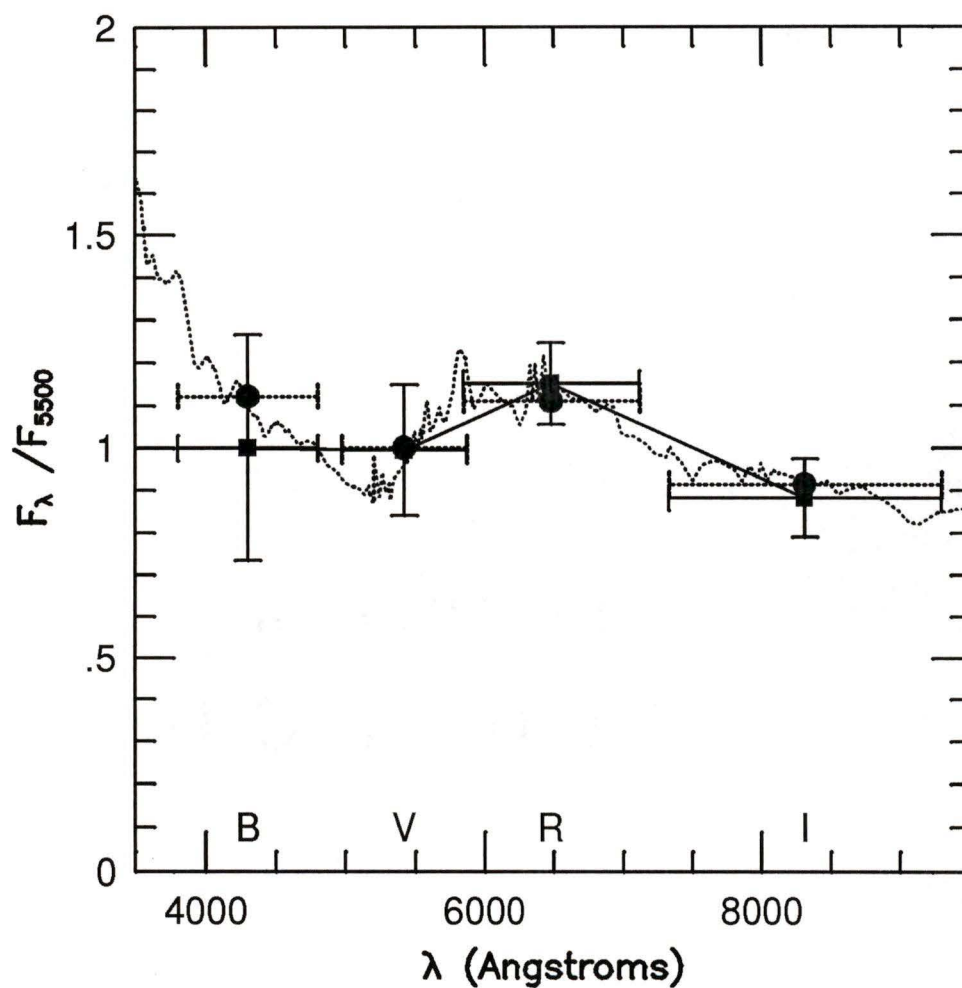


Figure 4.7: As Figure 4.6. The spectroscopic redshift of the galaxy this figure is 0.464; the template is of morphological type  $m = 0.37$  (roughly Hubble type Sc) and redshift  $z = 0.45$ .

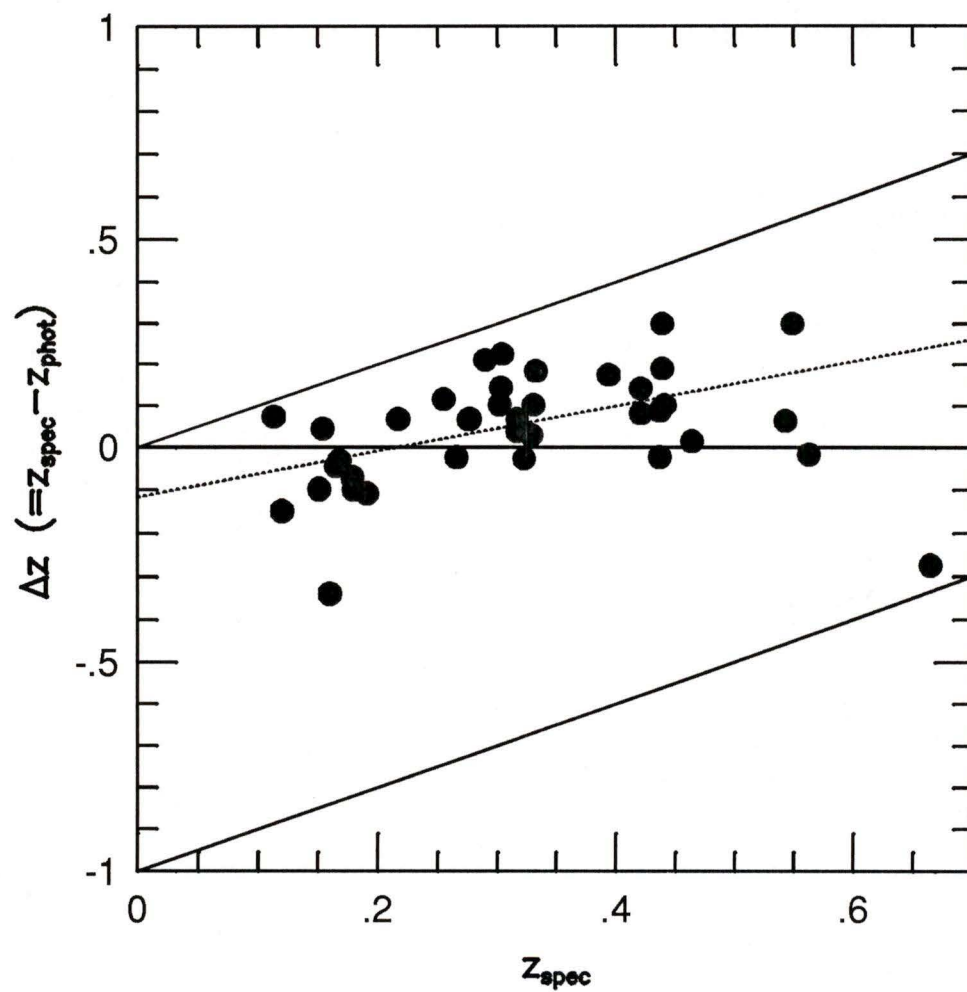


Figure 4.8: The trend of  $\Delta z$  with spectroscopic redshift. The solid lines indicate the limits of the photometric redshifts,  $0.0 < z_{\text{phot}} < 1.0$ . The dotted line is a least-squares fit to the points.

Table 4.3: Results from the basic photometric redshift technique: Part 1.

$$\Delta z = z_{spec} - z_{phot}$$

ID #	$z_{spec}$	$z_{phot}$	$\Delta z$	$m$
fB.11	0.191	0.30	-0.109	0.38
f5.12	0.302	0.20	0.102	0.54
f5.13	0.303	0.16	0.143	0.91
f5.14	0.304	0.08	0.224	0.99
f5.15	0.665	0.94	-0.275	0.39
f6.17	0.290	0.08	0.210	0.71
f6.19	0.394	0.22	0.174	0.79
f6.20a	0.437	0.46	-0.023	0.00
f6.20b	0.437	0.35	0.087	1.00
f4.21	0.266	0.29	-0.024	0.42
f4.22	0.549	0.25	0.299	0.00
f4.23	0.543	0.48	0.063	0.00
f4.24	0.277	0.21	0.067	0.51
f4.25	0.168	0.20	-0.032	0.89
f4.27	0.151	0.25	-0.099	0.33
f4.28	0.179	0.25	-0.071	0.38
f4.30	0.180	0.28	-0.100	0.00
f4.31	0.160	0.50	-0.340	0.52
f7.32	0.113	0.04	0.073	0.16
f7.33	0.331	0.23	0.101	0.89
f7.34	0.217	0.15	0.067	0.78
f7.36	0.421	0.28	0.141	0.99
f7.37	0.165	0.21	-0.045	0.53
f7.38	0.317	0.28	0.037	0.99
f7.39	0.439	0.14	0.299	1.00
f7.40	0.329	0.30	0.029	1.00
f7.41	0.255	0.14	0.115	0.10
f7.42	0.317	0.25	0.067	0.46
f7.43	0.333	0.15	0.183	0.85
f7.44	0.464	0.45	0.014	0.37

Table 4.4: Results from the basic photometric redshift technique: Part 2.

ID #	$z_{spec}$	$z_{phot}$	$\Delta z$	$m$
f7.45	0.421	0.34	0.081	1.00
f7.46	0.563	0.58	-0.017	0.58
f5.48	0.120	0.27	-0.150	0.37
fB.50	0.276	0.21	0.066	0.00
fB.51	0.441	0.34	0.101	1.00
fB.52	0.323	0.35	-0.027	0.20
fB.53	0.439	0.25	0.189	0.96
f6.54	0.154	0.11	0.044	0.00

This is not the whole story, however. The skew to positive values of  $\Delta z$  at the high redshift end of Figure 4.8 cannot be explained by the preceding argument, since at  $z_{spec} = 0.5$  the effects of redistribution from the high and low photometric limits cancel each other out. Also the trends in the work of Koo (1985) and Loh and Spillar (1986b) cannot be explained by this argument. The following chapter will endeavour to show that the trends can be explained by the evolution of the spectral energy distribution of galaxies with look-back time.

# Chapter 5

## Evolution

We know that the galaxies evolve. A redshift of  $z = 0.32$  (the average redshift of the sample) corresponds to a look-back time of 2.4 to 4.7 Gigayears and  $z = 1$  (the maximum photometric redshift available) corresponds to a look-back time of 4.8 to 9.6 Gigayears, depending on one's choice of the Hubble constant,  $H_0$  and cosmology. Over this much time, models show that the spectral energy distribution of galaxies does change (Bruzual, 1985; Yoshii and Takahara, 1988). Further, colour number count observations for faint ( $21 < B < 24$ ) galaxies also show differences with respect to the no-evolution predictions (Metcalf et al., 1991).

Thus it is hardly surprising that not allowing for the evolution of the spectral energy distributions of galaxies with redshift leads to errors in the photometric redshifts. What is needed is a method that accounts for evolution by modifying the templates.

## 5.1 Theoretical evolution

There are a number of theoretical models describing the evolution of the spectral energy distribution of galaxies in the literature. These models make various assumptions about the star formation rate, the initial mass function of stars and the cut-off time of star formation. Elliptical galaxies are usually described as galaxies that underwent a burst of star formation in the distant past but are no longer active. Rather, all evolution is now of the passive variety, with stars evolving and dying, but no new stars forming. The model for spiral galaxies is one of continuous active star formation, usually with some slow decay in the rate as less material is available to form stars.

In terms of spectral evolution, the early type (elliptical) galaxies evolve more than the later types (the spirals). This might seem to be counter-intuitive, as one normally considers elliptical galaxies to be quiet, non-starforming systems while spirals tend to be more active. If an early type galaxy is considered to be one which underwent a single burst of star formation at some early epoch, then the models show that these objects should show relatively large spectral evolution. As the early type galaxies age, their stellar population becomes redder and dimmer, rapidly at first, then slower when the light from low mass stars dominates. On the other hand, late type galaxies which are forming stars at a more continuous, leisurely pace are predicted to show much less spectral evolution.

The established models of galaxy evolution of Arimoto and Yoshii (1986; 1987), as summarized in Figure 2 of Yoshii and Takahara (1988), were used. The relevant, low redshift, section of that figure is reproduced in Figure 5.1.

It shows the change in the rest frame *UBVRI* magnitudes as a function of galaxy age,  $T_g$ . The early type galaxies can be seen getting much brighter with look-back time (fainter with age) while the late type galaxies show very little evolution.

Figure 5.1 shows the colour evolution of galaxies in terms of changes in magnitude with respect to one point: the present epoch. Obviously, the age of the galaxies at the present epoch depends on the epoch of galaxy formation and on the age of the universe. Yoshii and Takahara (1988) assume an epoch of formation of 15.5 Gigayears ago and a Hubble constant of  $H_0=50 \text{ km sec}^{-1} \text{ Mpc}^{-1}$  yielding an age of the universe of 17.5 Gyrs for  $q_0 = 0.05$  (a redshift scale for this choice of cosmology is shown on the bottom of Figure 5.1). However, any cosmology and epoch of formation can be used by calculating the new age of the galaxies at the present epoch and referring all magnitude shifts to that age. Thus, if  $H_0=100 \text{ km sec}^{-1} \text{ Mpc}^{-1}$  and the galaxies are assumed to have formed almost directly after the Big Bang (as indicated by the upper of the two redshift scales on Figure 5.1), the shift in *B* magnitudes from  $z = 0.0$  to  $z = 0.5$  is

$$\Delta B = B_{0.5} - B_{0.0} = (-1.7) - (-0.9) = -0.8, \quad (5.1)$$

for example. One can do this for all redshifts. For different morphologies one must interpolate between the magnitude shifts for the elliptical (E/S0) and disk (Sdm) galaxies.

The shifts in the *UBVRI* magnitudes are equivalent to changes in the flux at the central wavelengths of those filters. The changes in flux are very smooth functions of wavelength; it is possible to interpolate between the cen-

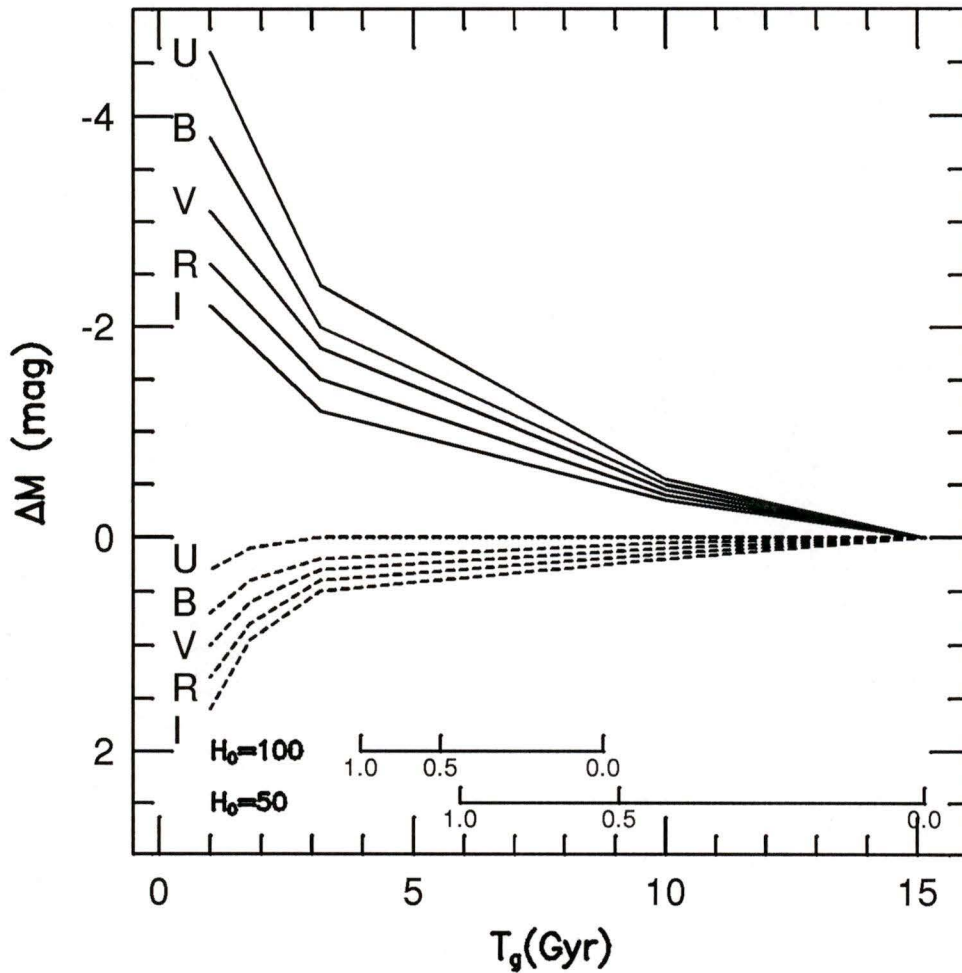


Figure 5.1: The spectral evolution of galaxies reproduced from Figure 2 of Yoshii and Takahara (1988). The figure shows the evolution in the rest frame *UBVRI* passbands of E/S0 (solid lines) and Sdm (dashed lines) galaxies as a function of galaxy age,  $T_g$ . Redshift scales are shown at the bottom of the figure for  $H_0=50$  and  $100 \text{ km sec}^{-1} \text{ Mpc}^{-1}$ ;  $\lambda_0 = 0.0$  and  $q_0 = 0.05$  in both cases.

tral wavelength of each filter and to extrapolate shortwards of  $U$  at  $3600\text{\AA}$  to  $2150\text{\AA}$ , the central wavelength of  $B$  for galaxies at  $z = 1$ . Since magnitudes are logarithms of fluxes, adding a shift to a magnitude corresponds to multiplying the flux by a factor (see equation 4.2). Thus the  $UBVRI$  magnitude shifts can be converted to a factor,  $f(\lambda)$  multiplying the rest frame fluxes,  $F(\lambda)$  of the template spectra at each wavelength to provide the modified template spectra  $F'(\lambda)$ ,

$$F'(\lambda) = F(\lambda)f(\lambda), \quad (5.2)$$

which now include the effects of evolution. The spectra are then redshifted and reduced to four fluxes as described in Section 4.2.

The modified templates were used to find photometric redshifts using the comparison method described in Section 4.3. The residuals,  $\Delta z = z_{spec} - z_{phot}$ , were calculated. They are shown as a function of spectroscopic redshift in Figure 5.2. The slope noted in the Section 4.4 is significantly reduced from a slope of  $b = .54$  to a slope of  $b = .22$  when evolution is incorporated. The standard deviation remains unchanged.

## 5.2 Empirical evolution

The empirical way to correct the templates is to compare them with the observed galaxies, measure the differences between them, and modify the templates to minimize these differences.

The SED's of the templates have all been normalized such that the flux at the central wavelength of the  $V$  passband,  $F_V$ , is unity. Thus the templates, in their reduced form, can be described by three flux ratios:  $F_B/F_V$ ,  $F_R/F_V$ ,



and  $F_I/F_V$ . Since the templates are defined at every point from  $m = 0$  to  $m = 1$  and from  $z = 0$  to  $z = 1$ , they can be visualized as surfaces in three dimensions of the form  $F_i/F_V = f(m, z)$  where  $i$  is one of the  $B$ ,  $R$  or  $I$  passbands. Figure 5.3 shows such a surface.

To compare properly the template SED's and those of the observed galaxies, it is necessary to find the morphology of the observed galaxies. The best way to determine the spectral Hubble type of a galaxy of known spectroscopic redshift and  $BVRI$  magnitudes is to use a variant on the basic photometric redshift procedure laid out in the Chapter 4. The first part of the method is the same: the magnitudes of the galaxy are converted into a SED. Instead of comparing this SED to all the 10 201 templates, only the 101 templates of different morphologies,  $m$ , at the redshift,  $z$ , nearest the spectroscopic redshift are considered. The morphology of best matching template is then a very good estimate of the morphology of the galaxy. Figure 5.3 shows  $m$ , the morphology thus determined,  $z$ , the spectroscopic redshift, and  $F_B/F_V$ , one of the flux ratios. The grid represents the templates while the observed galaxies are shown as filled circles.

Although it is somewhat difficult to tell from the figure, the observed points show a slight but systematic shift from the surface of the templates. The exact difference can be found for each observed galaxy. This gives the difference between the observed galaxies as a function of  $m$  and  $z$  at selected points. To provide a generalized description of the difference at all points, it is necessary to fit some sort of function to the points.

The simplest function possible would be to determine the average differ-

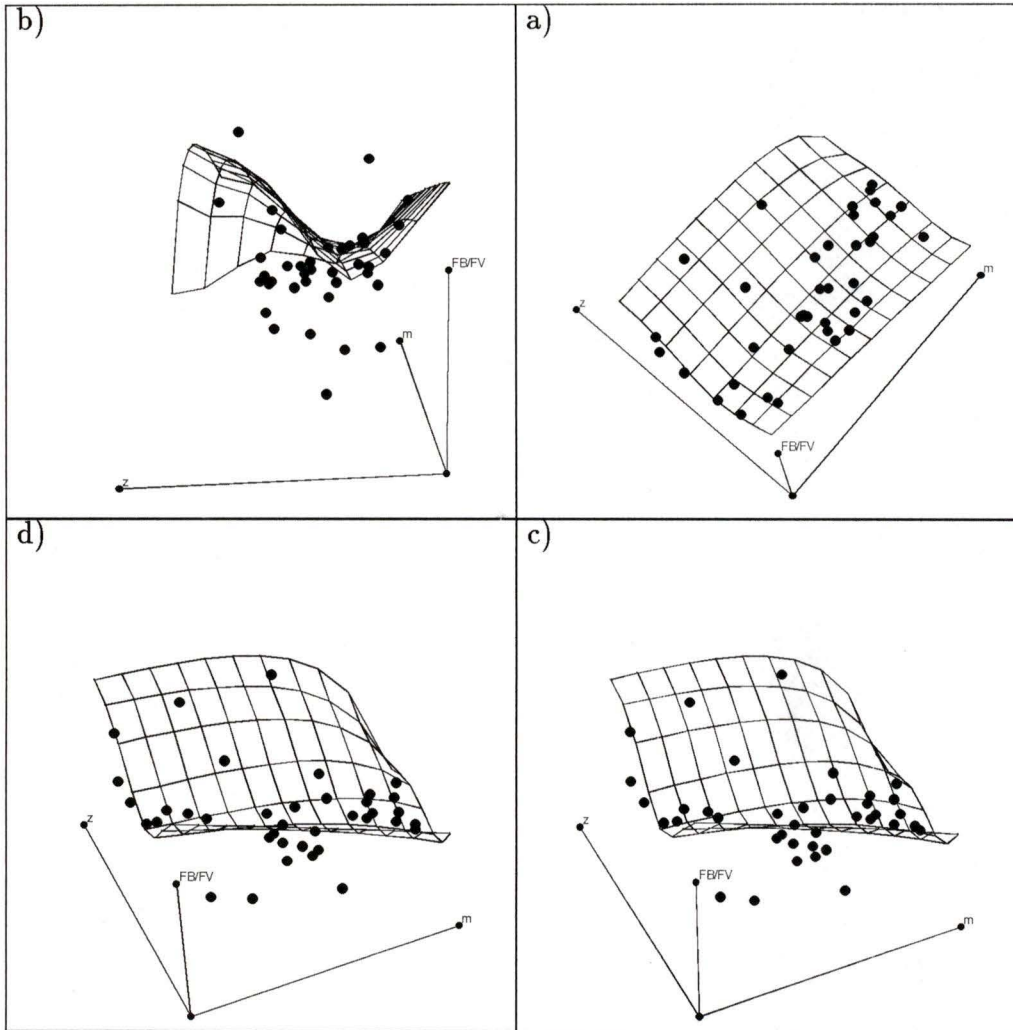


Figure 5.3: Four views of the flux ratio,  $F_B/F_V$ , as a function of morphology,  $m$ , and redshift,  $z$ . The grid represents the templates. Each square is  $.1$  in  $m$  by  $.1$  in  $z$ . The tip of vertical axis represents  $F_B/F_V = 1$ . The points represent the observed galaxies.

ence to between the observed points and the template surface:

$$D(m, z) = a_0 = \frac{1}{N_{gal}} \sum_{i=1}^{N_{gal}} (F_i - T(m_i, z_i)) \quad (5.3)$$

where  $a_0$  is the average difference  $D(m, z)$  is the difference plane,  $F_i$  is the flux ratio of the  $i$ th observed galaxy,  $T(m_i, z_i)$  is the flux ratio of the template at  $m_i, z_i$ , the morphology and redshift of the  $i$ th observed galaxy and  $N_{gal}$  is the number of observed galaxies, in this case, 38. This approach, however, is overly simple. It obviously does not describe any evolution since there is no dependence on redshift. The approach was tried but did not significantly improve the trend seen in Figure 4.8. That the trend is not improved by adding a constant to the templates in each flux ratio is reassuring because it indicates that there are no systematic errors in the calculation of the photometric colours of the observed galaxies.

The next simplest function is to fit a plane, a linear function of  $z$  and  $m$ , to the differences:

$$D(m, z) = a_0 + a_1 m + a_2 z \quad (5.4)$$

where  $a_0, a_1$  and  $a_2$  are constants. Since there is a dependence on redshift, modifications of this nature can represent evolutionary corrections. The constants are slightly harder to determine than in equation 5.3, but can be found easily enough by setting to zero the derivatives with respect to  $a_0, a_1$  and  $a_2$  of the following expression:

$$\sum_{i=1}^{N_{gal}} [(F_i - T(m_i, z_i)) - (a_0 + a_1 m + a_2 z)]^2 \quad (5.5)$$

and solving the resulting set of equations using linear algebra. Having obtained  $a_0$ ,  $a_1$  and  $a_2$  for each of the three flux ratios, the templates can be corrected:

$$T'(m, z) = T(m, z) + D(m, z) \quad (5.6)$$

where  $T'(m, z)$  represents the empirically corrected templates.

When photometric redshifts are determined using the empirically corrected templates, an improvement in the accuracy is found. Figure 5.4 shows a plot of  $\Delta z$  vs.  $z_{spec}$  for the empirically corrected templates; the least squares slope of the data is only  $b = .31$ . The standard deviation of  $\sigma = 0.127$  remains unchanged.

A valid concern when empirically modifying the templates in this manner is that the corrections might not be global. It is conceivable that the corrections improve the photometric redshifts only for the set of galaxies that was used to determine the corrections. To see if this is indeed the case, another set of galaxies is called for. Tables 4a through 4f of Pickles and van der Kruit (1991) were searched for those field galaxies which had a complete set of *BVRI* photometry and spectroscopic redshifts. These data are shown in Table 5.1. When photometric redshifts are determined for the Pickles and van der Kruit (1991) data, the redshift residuals,  $\Delta z$ , are distributed in exactly the same way as the residuals from the data of Chapter 3. The Pickles and van der Kruit redshift residuals are shown as open circles in Figure 5.4. They have the same distribution as the redshift residuals as the original data. This confirms that the empirical modifications to the templates apply to galaxies in general and not just the one sample of galaxies in particular.

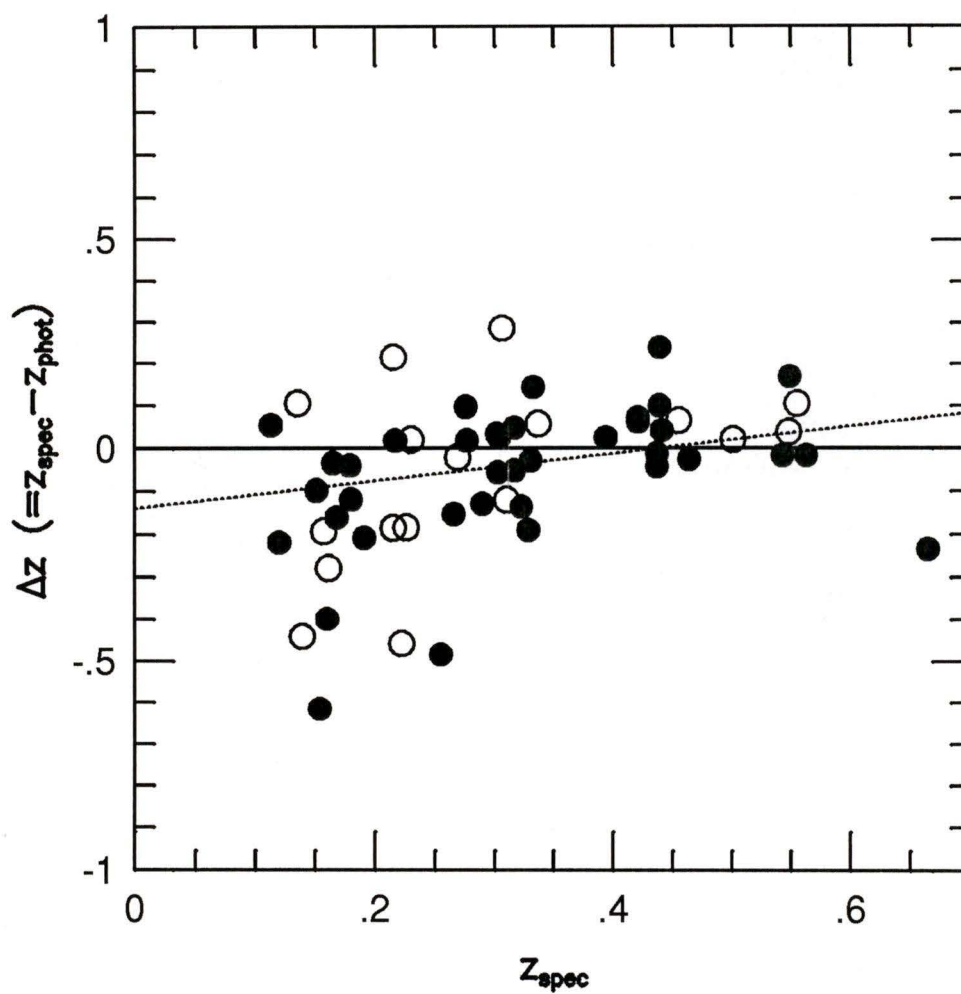


Table 5.1: Additional photometric and redshift data from Pickles and van der Kruit (1991)

Table	ID#	$z$	$B$	$V$	$R$	$I$
4a	43	0.139	21.040	20.010	19.305	18.400
4a	90	0.161	22.775	21.635	20.730	19.935
4a	106	0.555	23.575	22.485	21.470	20.955
4a	109	0.455	23.015	21.370	20.345	19.365
4a	120	0.215	22.600	21.500	20.875	20.070
4a	121	0.215	22.555	21.590	20.905	20.185
4a	134	0.299	22.265	21.030	18.825	17.410
4b	34	0.306	21.835	20.585	19.975	19.125
4b	40	0.226	22.410	21.240	20.405	19.605
4b	54	0.222	22.100	21.185	20.750	19.830
4b	102	0.548	23.685	21.885	20.715	19.640
4b	103	0.310	22.420	21.735	21.260	20.970
4b	116	0.230	22.345	21.470	21.085	20.600
4b	125	0.135	20.100	18.800	18.205	17.360
4c	138	0.501	24.695	22.895	21.420	20.195
4e	46	0.337	21.290	19.875	19.175	18.675
4e	56	0.157	21.930	21.005	20.590	20.425
4f	110	0.269	21.445	19.905	19.150	18.445

### 5.3 Error distributions

Although allowing for the evolution of galaxies over look-back time and modifying the templates accordingly makes the discrepancies between photometric and spectroscopic redshifts smaller, neither theoretical nor empirical corrections provide a perfect match. Although both kinds of corrections reduce the least-squares slope of the redshift residuals,  $\Delta z = z_{spec} - z_{phot}$ , with respect to spectroscopic redshift, neither of them reduce it to zero. This is because

the least-squares method for determining the slope is not completely valid in this instance. The least-squares method for determining the slope of some data assumes that the errors in the data are Gaussian in nature.

If the photometric redshift technique could return values of  $z_{phot}$  greater than  $z_{phot} = 1$  or less than  $z_{phot} = 0$ , then the errors in the redshift residuals of Figures 4.8, 5.2 and 5.4 would be Gaussianly distributed. But this is not the case; there are upper and lower limits on the photometric redshifts, and hence on the redshift residuals. At a given  $z_{spec}$ , the redshift residual,  $\Delta z = z_{spec} - z_{phot}$ , cannot be greater than  $\Delta z = z_{spec}$  or less than  $\Delta z = z_{spec} - 1$ . Because Gaussian distributions have infinite tails in either direction, the redshift residual error distributions are not Gaussian.

The question now is “What is the form of the redshift residual error distributions?” One can imagine several possibilities for the fate of those photometric redshifts that would lie by chance at redshifts greater than  $z = 1$  or less than  $z = 0$  if templates were available for those areas:

1) It could be that the technique returns the nearest available redshift to the redshift that would have been chosen had templates been available. Thus if, by chance, the photometric redshift would have been negative, a photometric redshift of  $z_{phot} = 0$  would be returned. In this case, the redshift residuals would have a distribution resembling a truncated Gaussian with delta functions at each end.

2) The photometric redshift technique works by minimizing  $\chi^2$  as a function of  $m$  and  $z$ . There are, generally, more than one local minima in the  $m - z$  surface. It is possible that, if the deepest minimum lay at an impossible redshift, the second deepest minimum would lie at a possible redshift.

If this were the case, this “second guess” might well lie close to the true value. The error distribution of this second redshift might be typical of the original error distribution. In this case, the redshift residuals would have a distribution resembling a truncated Gaussian multiplied by a constant.

3) Another possibility is that the second minimum bears no relation to the correct redshift. In this case, the “second guess” would be a random number between 0.0 and 1.0. In this case, the redshift residuals would have a distribution resembling a truncated Gaussian plus some constant.

These possibilities are illustrated in Figure 5.5. The filled dots are distributed evenly between  $z_{spec} = 0$  and  $z_{spec} = 1$ . In the  $\Delta z$  direction, they are distributed with a Gaussian centred on  $\Delta z = 0$ ;  $\sigma = .25$  is the standard deviation. This is not intended to mimic exactly the observed redshift error distribution, which has no redshifts higher than  $z = .7$  and whose standard deviation is smaller by half, but merely to illustrate some possible redistributions. Redistributed points are shown as open circles with arrows leading from the original points. Figure a) shows the points with no redistribution. Figure b) shows the points shifted to the nearest allowed redshift as described in 1) above. Figure c) illustrates a Gaussian redistribution as per 2) above. Figure d) shows an even redistribution as described in point 3).

Two kinds of simulations were used to determine which of the three redistribution possibilities best described the observed redshift error distribution. The first was relatively simple. Random spectroscopic redshifts were generated with a distribution similar to that of the real sample. Random photometric redshifts were generated by adding a Gaussian distribution with varying values of  $\sigma$  to the spectroscopic redshifts. Any points lying at

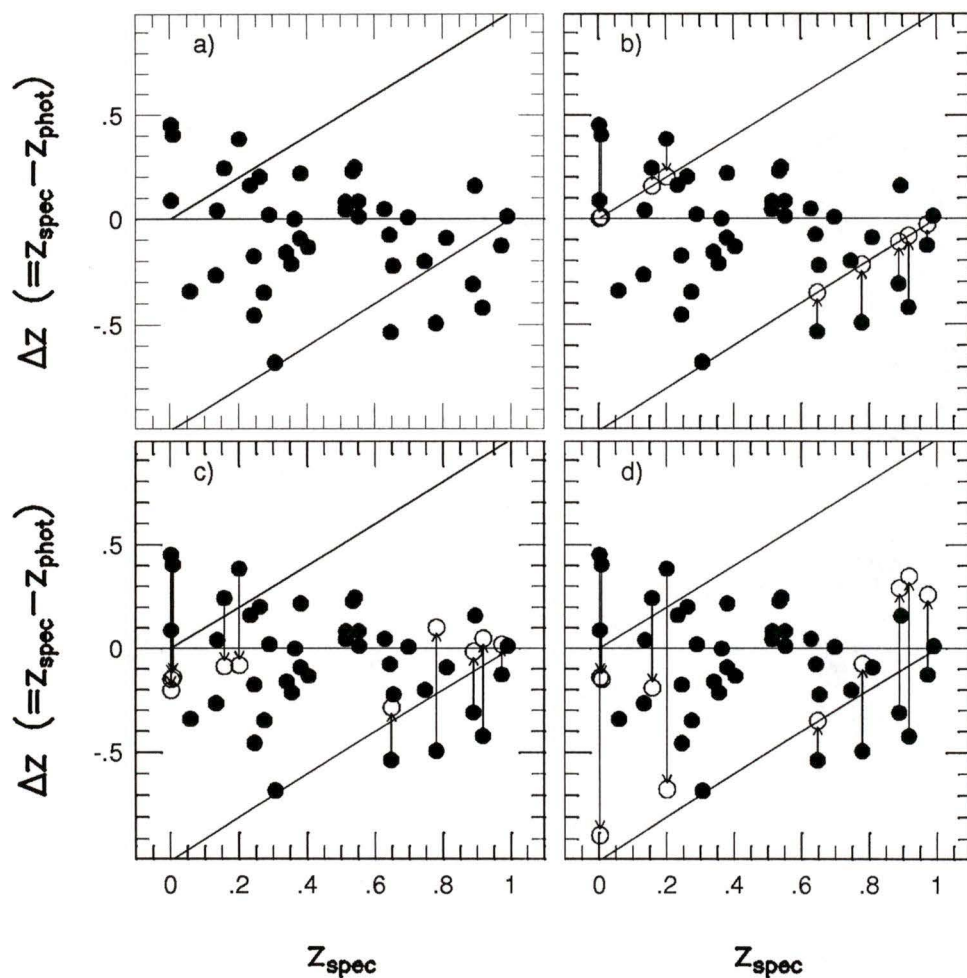


Figure 5.5: Possible error distributions. The filled circles show a Gaussian spread about  $\Delta z = 0$ . The diagonal lines show the permitted range of redshift residuals. Those points lying outside the diagonal lines have arrows pointing to open circles indicate possible redistributions. Figure a) shows no redistribution, b) a clipped redistribution c) a Gaussian redistribution d) a boxcar redistribution.

photometric redshifts greater than  $z_{phot} = 1$  or less than  $z_{phot} = 0$  were redistributed in one of the three ways described above. The standard deviation (not necessarily the same as the input  $\sigma$ ) and the least squares slope of the resulting  $z_{spec}$  vs.  $\Delta z$  distribution were then calculated and plotted against each other. Increasing the input  $\sigma$  will directly increase the standard deviation of the resulting distribution and indirectly increase the least squares slope by causing more points to lie outside the permitted region and hence be redistributed. For each value of  $\sigma$ , the simulation was run 5000 times with 40 points per run and the results averaged. The results of these redistribution simulations are shown as solid lines in Figure 5.6. As can be seen, when no redistribution occurs, the least squares slope never deviates from zero. However when redistribution does occur, the least squares slope increases with standard deviation at different rates depending on the redistribution method.

The second set of simulations tested the accuracy of the photometric redshift technique as the errors in the photometry,  $\Delta M$ , were increased. For each value of  $\Delta M$ , the following procedure was repeated 100 times. Forty templates were chosen at random from the 10 201 templates available. There was an equal chance of choosing any of the 101 morphologies,  $m$ . The redshifts were chosen with a distribution similar to the real redshift distribution. Each template was converted into a set of  $BVRI$  magnitudes. To simulate observational errors, a small random number distributed with a Gaussian of width  $\Delta M$  was added to the magnitudes. Photometric redshifts were determined from the resulting “ $BVRI$  photometry” of these 40 “galaxies” in the manner described in Chapter 4. These photometric redshifts were compared

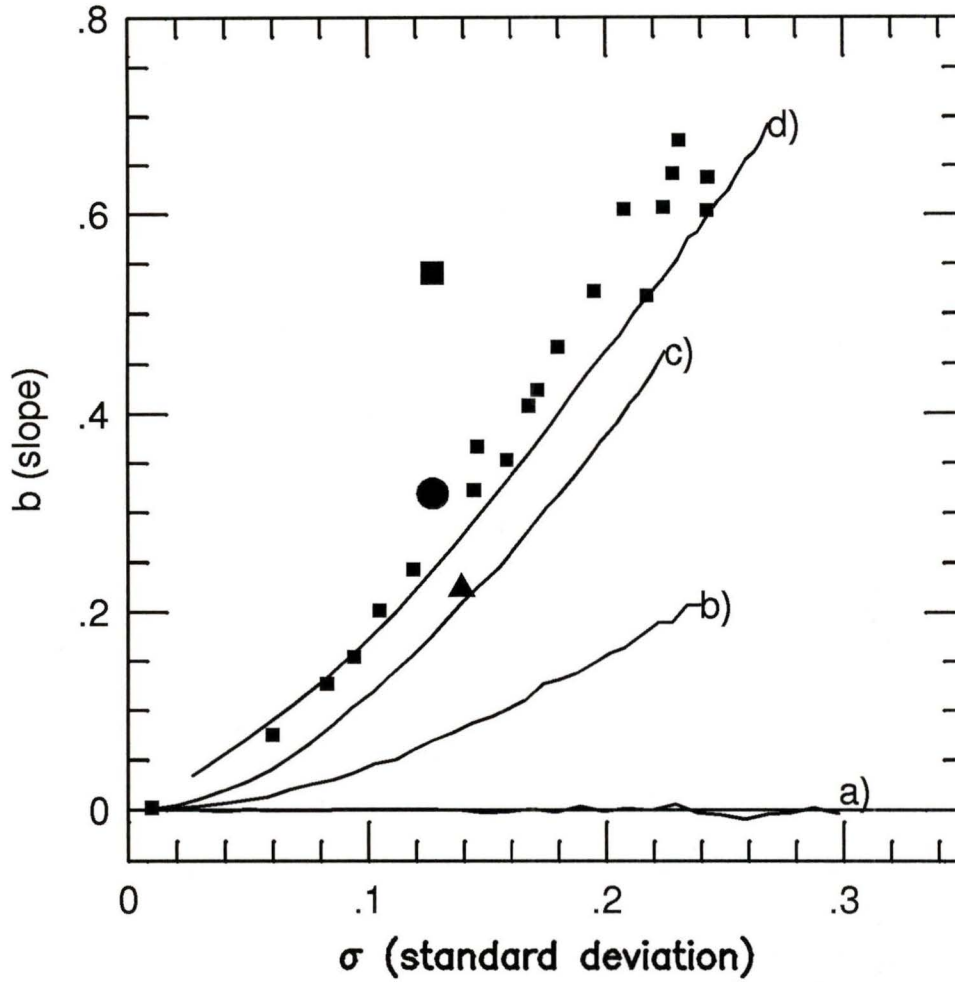


Figure 5.6: Simulation results. The lines show the results of the redistribution simulations for different kinds of redistribution: Line a) shows no redistribution, b) a clipped redistribution c) a Gaussian redistribution d) a boxcar redistribution. The small squares show the results of the photometric redshift simulations. The large symbols show the points occupied by the measured redshift residuals. Square: uncorrected (Fig. 4.8) Triangle: theoretically corrected (Fig. 5.2) Circle: empirically corrected (Fig. 5.4).

with the redshifts of the templates from which they were derived. The standard deviation and least squares slope were determined in the same way that the photometric redshifts were compared to the spectroscopic redshifts for the real data. For each value of  $\Delta M$ , the 100 results were averaged.

Not surprisingly, when the errors in the photometry were zero, the photometric redshift technique always picked the correct redshift. As the errors in the photometry,  $\Delta M$ , increased, so did the errors in the photometric redshifts in the form of the standard deviation of redshift residuals and an increase in standard deviation leads to an increase least squares slope of redshift residuals. The question is which of the redistribution schemes outlined above describes what is happening in the redshift simulations and, one presumes, real life. The results of these photometric redshift simulations are shown as small squares on Figure 5.6. The redistribution simulation that best matches the photometric redshift simulation is the even random redistribution scheme described in paragraph 3) above. The rate at which slope increases with standard deviation in this simulation is very similar to the rate of the redshift simulations.

Figure 5.6 also shows the values of the standard deviation and least squares slope of the redshift residuals resulting from the uncorrected templates, the templates corrected for theoretical evolution, and the empirically corrected templates as a large square, a triangle and a circle respectively. Both the points corresponding to the theoretically and empirically corrected templates lie close to the photometric redshift simulations and the even random redistribution simulation. They also lie near the photometric redshift simulation corresponding to  $\Delta M = 0.05$  which is roughly the photometric

uncertainty associated with the real data. It is concluded, therefore, that:

- 1) Evolution does account for part of the skew in the redshift residuals.
- 2) Adding evolution to the original templates based on  $z = 0$  galaxies using either theoretical models or empirical corrections produces a set of templates that represent a good match with the observed galaxies.
- 3) If, through the vagaries of Gaussian error distribution, a photometric redshift would have been determined to be negative or greater than 1.0, then the photometric redshift technique returns a redshift that is completely uncorrelated with the actual redshift.
- 4) Photometric errors can account for that part of the trend not accounted for by evolution.

# Chapter 6

## Luminosity functions

The redshift determination was found to be accurate to within  $\pm .125$  in  $z$  ( $1 \sigma$ ). Compared to spectroscopic redshifts, where typically  $\Delta z \sim 0.001$ , the uncertainties associated with photometric redshifts are large. However, simulations indicate that this level of precision is sufficient to calculate a fairly accurate luminosity function. The luminosity function is the number of galaxies per cubic megaparsec per magnitude interval as a function of absolute magnitude.

### 6.1 The sample

The CCD frames containing the Colless galaxies also contained a much larger number of galaxies whose spectroscopic redshifts are unknown. The templates corrected for theoretical evolution were used to determine a photometric redshift for every galaxy in the frames. In all, redshifts were determined for 291 galaxies. The sample of galaxies is complete to  $B < 22.5$  and  $R < 20.5$ . A subsample was constructed containing galaxies that satisfied ei-

ther completeness condition. Galaxies with  $z < 0.15$  were excluded from the sample so that only the high redshift population would be represented. This subsample contained 187 galaxies. For the galaxies in the subsample that had spectroscopic redshifts, the spectroscopic redshifts were used instead of the photometric redshifts. The average redshift of the subsample is  $z = 0.34$ .

## 6.2 The $1/V_a$ method

From this subsample, luminosity functions were constructed using the  $1/V_a$  method. The  $1/V_a$  method is well known (Schmidt, 1968) and has been described in detail elsewhere (Schade, 1990) so the following description will be brief.  $V_a$  is defined as the volume accessible to a galaxy given its absolute magnitude and the limits defining the sample in which it is found. Formally,

$$V_a = \int_{z_{min}}^{z_{max}} \frac{dV}{dz} dz, \quad (6.1)$$

where  $dV/dz$  is the co-moving differential volume element:

$$\frac{dV}{dz} = \frac{4\pi c d_L^2}{H_0(1+z)^3(1+2q_0z)^{1/2}}. \quad (6.2)$$

The luminosity distance  $d_L$  is given by equation 1.3.

The limits,  $z_{min}$  and  $z_{max}$  can be fixed (as in a volume limited sample), but for a magnitude limited sample they must be determined for every galaxy. Given the absolute magnitude,  $M$ , of each galaxy and the limiting apparent magnitude of the sample,  $m_{lim}$ , the maximum redshift at which the galaxy would still be in the sample,  $z_{max}$ , can be determined by solving the following equation:

$$m_{lim} = M + \mu(z_{max}) + k(z_{max}). \quad (6.3)$$

where  $\mu(z_{max})$  is the distance modulus corresponding to  $z_{max}$  and  $k(z_{max})$  is the k-correction term. Two types of k-corrections were used : when possible, empirical k-corrections were determined from the spectral energy distribution derived from the *BVRI* photometry. Otherwise, the k-corrections given in Metcalfe *et al.* (1991) were used. Finally, to determine the luminosity function,  $\Phi$ , one uses the equation:

$$\Phi(M) = \frac{4\pi}{A} \sum_{M-\frac{\Delta M}{2}}^{M+\frac{\Delta M}{2}} \frac{1}{V_a}, \quad (6.4)$$

where  $A$  is the area surveyed (in steradians) and  $\Delta M$  is the binsize used. In the present case,  $z_{min} = .15$  for all galaxies and  $z_{max}$  is determined for each galaxy using equation 6.3 with  $m_{lim} = B = 22.5$  or  $m_{lim} = R = 20.5$ .

The assumed cosmology was one where  $H_0 = 75 \text{ km sec}^{-1} \text{ Mpc}^{-1}$ ,  $\Omega_0 = .1$ , and  $\lambda_0 = 0$ . Changing the values of  $\Omega_0$  and  $\lambda_0$  has very little effect on the shape of the luminosity functions. Changing  $H_0$  does not significantly affect the shape of the luminosity functions but does cause shifts along both axes: a shift of  $5 \log h_{75}$  on the horizontal magnitude axis and  $3 \log h_{75}$  on the vertical space density axis. Here  $h_{75} = H_0/75 \text{ km sec}^{-1} \text{ Mpc}^{-1}$ .

### 6.3 The luminosity function

The  $B$  luminosity function derived by the above method is shown in Figure 6.1 along with Eales' (1993)  $B$  luminosity function for  $.15 < z < .4$  and Lonsdale & Chokshi's (1993) luminosity function for a similar redshift range. The error bars shown only reflect the Poisson  $1/\sqrt{N}$  fluctuations, where  $N$  is the number of galaxies in each bin. Uncertainties in the luminosity function

due to the errors in the redshifts and magnitudes will increase the size of the error bars.

There is good agreement between the photometric redshift luminosity function and those of Eales (1993) and Lonsdale & Chokshi (1993) for moderate redshift. Both these luminosity functions were calculated using  $\sim 500$  spectroscopic redshifts from various sources (Peterson et al., 1986; Broadhurst et al., 1988; Colless et al., 1990; Cowie et al., 1991). The total observing time required was about 40 hours on 4-metre class telescopes. Only 2 hours were needed to measure almost 300 photometric redshifts and determine the same luminosity function. Although the comparatively low accuracy of photometric redshifts makes them of limited use for measuring the properties of a single galaxy, they can be used to determine the properties of a large number of galaxies quite effectively, as this luminosity function demonstrates.

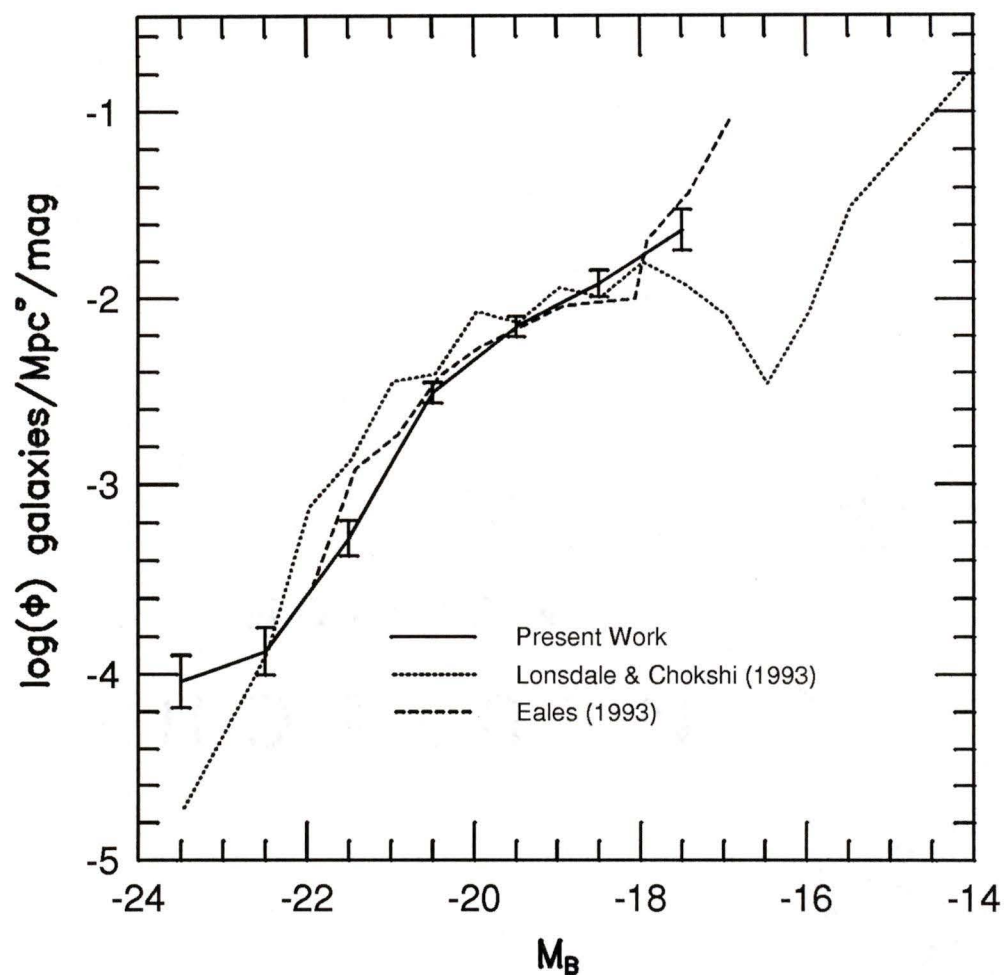


Figure 6.1: The medium redshift  $B$  luminosity function derived from photometric redshifts compared with two other high redshift luminosity functions from the literature. The error bars represent  $1/\sqrt{N}$  uncertainties which underestimate the true uncertainties, particularly in the brightest and dimmest magnitude bins. A value of  $75 \text{ km sec}^{-1} \text{ Mpc}^{-1}$  is assumed for  $H_0$ .

# Chapter 7

## Conclusion

### 7.1 Summary

This thesis has presented a method to measure the redshifts of galaxies using broad-band photometry instead of spectroscopy. The method was tested with galaxies whose redshifts had been determined spectroscopically by Colless *et al.* (1990; 1993) and Boyle, Jones & Shanks (1991). *BVRI* photometry for these galaxies was obtained at CFHT. The *BVRI* magnitudes were converted into low resolution spectra which were then compared to template spectra in order to determine the redshift. This idea was not entirely new (see Loh and Spillar (1986b) for example) but two improvements were made: (1) The technique used a standard filter system which makes it accessible to a larger number of users. (2) The templates were not just redshifted copies of  $z = 0$  galaxies. They were modified to allow for evolution by either theoretical or empirical means. The resulting redshifts were found to have an accuracy of  $\Delta z = \pm .125$ .

Despite the relatively low precision of these photometric redshifts com-

pared with spectroscopic redshifts ( $\Delta z = \pm 0.001$ ) photometric redshifts do have applications. Almost three hundred photometric redshifts were measured. About two hundred of these were used to determine a luminosity function for field galaxies at  $\langle z \rangle \sim 0.3$ , which compares favourably with its spectroscopic counterparts. The observing time required to measure the necessary photometric redshifts was a factor of 20 less than the time required to measure the spectroscopic redshifts. This example demonstrates the advantages of photometric redshifts in projects where large number of redshifts are needed but low precision can be tolerated.

## 7.2 Future work

At magnitudes brighter than  $B = 23$ , spectroscopic redshift determinations require an integration of about an hour on a 4-metre telescope. On a similar telescope, the integration time would be about 5 minutes per filter to determine a photometric redshift. Hence, the resultant gain is only a factor of two or three in time per galaxy. However, photometric redshifts have another advantage in speed over spectroscopy: multiplexing. Because it is possible to determine a photometric redshift for every object in a CCD frame, hundreds of redshifts can be measured at once. As multi-object spectrographs (which can measure many redshifts simultaneously) become more and more common, this advantage is less important than it was only a few years ago when only one or two redshifts could be measured at once. As detector technology improves, it remains a relevant factor, however, because the number of galaxies multi-object spectrographs can observe at once and CCD sizes

( $4K \times 4K$  and up) are increasing at roughly the same rate. At fainter magnitudes the integration times to determine spectroscopic redshifts increase significantly faster than the length of photometric integrations. Unfortunately, at those fainter magnitudes, and hence larger redshifts, evolution has a much stronger effect on the shape of galaxy spectral energy distributions, making the photometric redshifts less accurate.

There are limits on the ultimate accuracy of photometric redshifts. If (1) perfect photometry is available for an object, and if (2) the intrinsic restframe spectral energy distribution of an object is perfectly known beforehand, then it is possible to obtain a perfect photometric redshift. (Indeed, as Koo (1985) points out, only two passbands are needed to determine a redshift in this hypothetical case.) However, if one of these two conditions is not met, then there will be some error in the photometric redshift. Although “perfect” photometry is impossible, it is possible to obtain high signal-to-noise photometry for galaxies. The simulations described in Section 5.3 can be used to find the effects of decreasing the signal-to-noise ratio (SNR) of the photometry on the accuracy of redshifts derived from this photometry. The results of the simulations are shown in Figure 7.1. As the SNR drops below about 10 ( $\Delta Mag \simeq .1$ ), the standard deviation of the redshift residuals starts to climb rapidly. Although it would seem that by increasing the SNR any redshift accuracy could be obtained, condition (2) comes into play. According to Pence (1976) and other sources, there is an intrinsic scatter of  $\Delta M \simeq .05$  in the colours of galaxies of each type. This corresponds to variation in the stellar populations in galaxies. This scatter in galaxy colours is equivalent to a maximum signal-to-noise ratio of 20 in the measured photometry. As can

be seen on Figure 7.1, this implies a minimum uncertainty of  $\sigma \simeq .12$  in the photometric redshifts.

Figure 7.1 also shows a shortcoming in the photometric redshift technique described in this thesis. The upper line shows the results of simulations of this technique based on *BVRI* photometry. The lower, dashed line, indicating much better precision ( $\Delta z = \pm .04$  at a signal-to-noise ratio of 20), is a simulation of the same technique but based on *UBVRI*. Having ultra-violet information is ultra-important. Indeed, a recent paper (Connolly et al., 1995) showed that merely performing a linear regression of the form

$$z = a_0 + a_1U + a_2B_J + a_3R_F + a_4I_N \quad (7.1)$$

is sufficient to determine accurate redshifts if  $U$  is one of the filters. The biggest consistent feature in galaxy spectra is the  $4000\text{\AA}$  break. Having extensive filter coverage on both sides of the  $4000\text{\AA}$  break greatly increases the accuracy of the photometric redshifts. The  $U$  filter ( $3600\text{\AA}$ ) provides this coverage. The  $B$  filter ( $4400\text{\AA}$ ) appears to be inadequate, even at higher redshifts, when it is shortwards of the break. All future photometric redshift techniques should include  $U$ . The original version of the photometric redshift technique presented here was to include  $U$ . Unfortunately, the ultra-violet quantum efficiency of the detector that was used to collect the data at CFHT (the Lick 2 CCD) was only  $\sim 1\%$ . Consequently, the required integration times would have been prohibitively long.

Most applications will require spectroscopic redshifts. The potential for increased accuracy and the advantage of speed, however, insure a niche for photometric redshifts as long as present detector technology trends continue.

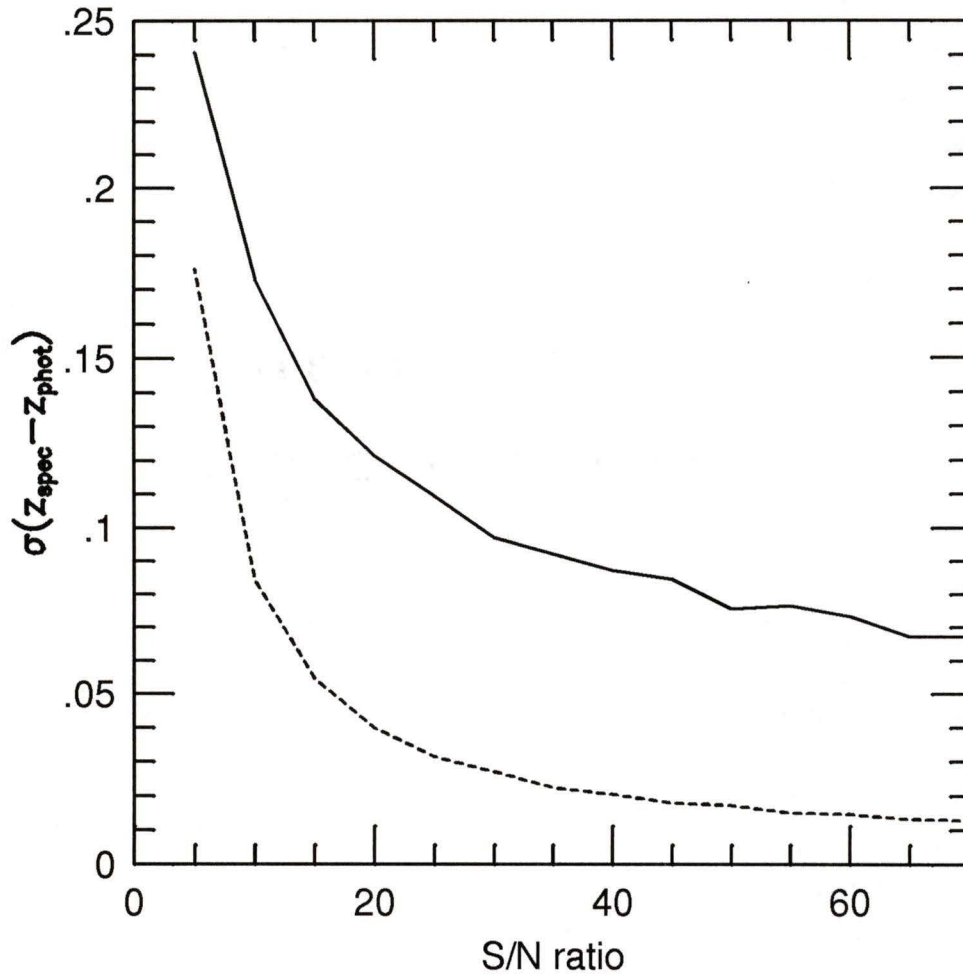


Figure 7.1: The results of simulations showing the effect of photometric errors on photometric redshift errors. The standard deviation of photometric redshift residuals is plotted against photometric signal-to-noise ratio. The upper line shows the results of the *BVRI* simulations. It corresponds to photometry used in this thesis. The lower, dashed line shows the simulation where all *UBVRI* magnitudes are incorporated. It indicates the importance of *U* magnitudes for measuring photometric redshifts.

Further, the concept of turning multi-passband photometry into spectral energy distributions complements spectroscopic redshifts very nicely. Knowing the SED of a galaxy is useful for two reasons.

First, it allows the empirical calculation of  $k$ -corrections. To measure the rest-frame properties of a galaxy or to calculate the luminosity function of a group of galaxies,  $k$ -corrections are necessary. Generally,  $k$ -corrections for galaxies have been calculated by (in order of decreasing accuracy): optically determining a morphology and assuming the corresponding SED; or assuming the galaxy has some average SED, usually that of an Sb galaxy. Empirical  $k$ -corrections are more accurate than any of these methods.

Second, knowing the spectral energy distribution of galaxies gives direct information about their stellar populations. Combined with the look-back times given by their redshifts, this allows one to trace the evolution of galaxies. This is not only intrinsically interesting, but also permits improvements to the photometric redshift methods. As was mentioned earlier, the accuracy of photometric redshifts at very faint magnitudes is limited because of evolution not accounted for by the template spectra. This can be circumvented, however, by observing this spectral evolutions and incorporating it into the templates.

The next generation of redshift surveys for galaxies fainter than  $B = 23$  is starting. The photometric redshift technique will be a valid tool for determining a large number of redshifts with very little observing time. This thesis shows that two things are important for determining accurate photometric redshifts:  $U$  magnitudes and evolution. The former can be included in any future photometric redshift technique quite easily, merely including  $U$  as one

of the observational bandpasses. The latter requires that several galaxies must be observed both spectroscopically and photometrically to determine the effects of evolution.

# Bibliography

- Arimoto, N. and Yoshii, Y.: 1986, *Astron. & Astrophys.* **164**, 260
- Arimoto, N. and Yoshii, Y.: 1987, *Astron. & Astrophys.* **173**, 23
- Baum, W. A.: 1962, in G. C. McVittie (ed.), *Problems of extra-galactic research*, p. 390, IAU Symposium No. 15
- Boyle, B. J., Jones, L. R., and Shanks, T.: 1991, *M.N.R.A.S.* **251**, 482
- Broadhurst, T. J., Ellis, R. S., and Shanks, T.: 1988, *M.N.R.A.S.* **235**, 827
- Bruzual, G. A.: 1983, *Astrophys. J.* **273**, 105
- Bruzual, G. A.: 1985, *Rev. Mex. Astron. Astrof.* **10**, 55
- Burstein, D. and Heiles, C.: 1982, *Astron. J.* **87**, 1165
- Colless, M. M., Ellis, R. S., Broadhurst, T. J., and Peterson, B. A.: 1993, *M.N.R.A.S.* **244**, 408
- Colless, M. M., Ellis, R. S., Taylor, K., and Hook, R. N.: 1990, *M.N.R.A.S.* **244**, 408
- Connolly, A. J., Csabai, I., Szalay, A. S., Koo, D. C., Kron, R. G., and Munn, J. A.: 1995, *Slicing through multicolour space: galaxy redshifts from broadband photometry*, Preprint
- Connolly, A. J., Szalay, A. S., Bershadsky, M. A., Kinney, A. L., and Calzetti, D.: 1994, *Spectral classification of galaxies: an orthogonal approach*,

## Preprint

- Cowie, L. L., Songaila, A., and Hu, E. M.: 1991, *Nature* **354**, 460
- Eales, S.: 1993, *Astrophys. J.* **404**, 51
- Illingworth, V.: 1985, *The facts on file dictionary of astronomy*, Facts on File, Inc., 2nd edition
- Johnson, H. L.: 1966, *Annual Review of Astronomy and Astrophysics* **4**, 193
- Kennicutt, R. C. J.: 1992, *Astrophys. J. Supp.* **79**, 255
- Koo, D. C.: 1985, *Astron. J.* **90**, 418
- Loh, E. D. and Spillar, E. J.: 1986a, *Astrophys. J.* **307**, L1
- Loh, E. D. and Spillar, E. J.: 1986b, *Astrophys. J.* **303**, 154
- Lonsdale, C. J. and Chokshi, A.: 1993, *Astron. J.* **105**, 1333
- Metcalf, N., Shanks, T., Fong, R., and Jones, L. R.: 1991, *M.N.R.A.S.* **249**, 498
- Monnet, G.: 1990, *Canada France Hawaii Telescope Observers Manual*, Canada France Hawaii Telescope Corporation, 4th edition
- Pence, W.: 1976, *Astrophys. J.* **203**, 39
- Peterson, B. A., Ellis, R. S., Efstathiou, G., Shanks, T., Bean, A. J., Fong, R., and Zen-Long, Z.: 1986, *M.N.R.A.S.* **221**, 233
- Pickles, A. J. and van der Kruit, P. C.: 1991, *Astron. & Astrophys. Supp.* **91**, 1
- Schade, D. J.: 1990, *Ph.D. thesis*, University of Victoria
- Schmidt, M.: 1968, *Astrophys. J.* **151**, 393
- Yoshii, Y. and Takahara, F.: 1988, *Astrophys. J.* **326**, 1

# Glossary

**BVRI:** Refers to photometry in the Blue (B:4400Å), Yellow (V:5500Å), Red (R:6500Å) and Infrared (I:8300 Å) regions of the spectrum.

**CCD:** Charge Coupled Device. A two dimensional photometric detector.

**CFHT:** Canada France Hawaii Telescope.

**E/S0/Sa/Sb/Sc/Irr:** Different galaxy morphologies from elliptical (E) through the different kinds of spiral (Sa/Sb/Sc) to irregular (Irr).

**FOCAM:** Prime Focus Camera at CFHT.

**IRAF:** Image Reduction and Analysis Facility. The most commonly used image analysis program in optical astronomy.

**SED:** Spectral Energy Distribution.

**SNR:** Signal to Noise Ratio.

**UJFN:** Refers to photographic photometry in Ultraviolet (U:3700Å), Blue (J:4600 Å), Red (F:6200 Å) and Infrared (N:7900 Å). regions of the spectrum. Sometimes written  $UB_JR_FI_N$ .

## VITA

Surname: Gwyn

Given Names: Stephen Donald Jermy

Place of Birth: Montreal, Quebec, Canada

### Educational Institutions Attended:

University of Victoria	1990 – 1995
McGill University	1987 – 1990

### Degrees Awarded:

B.Sc. (Honours) McGill University	1990
-----------------------------------	------

### Honours and Awards:

Graduate Teaching Fellowship	1991 – 1995
Bourse de maîtrise des Fonds FCAR	1990 – 1992
NSERC University Undergraduate Student Research Award	1989
Faculty Scholar, Faculty of Arts and Science	1987 – 1988


## Partial Copyright Licence

I hereby grant the right to lend my dissertation to users of the University of Victoria Library, and to make single copies only for such users or in response to a request from the Library of any other university, or similar institution, on its behalf or for one of its users. I further agree that permission for extensive copying of this dissertation for scholarly purpose may be granted by me or a member of the University designated by me. It is understood that copying or publication of this dissertation for financial gain shall not be allowed without my written permission.

### Title of Dissertation:

Photometric Redshifts: A Semi-Empirical Method

### Author:

  
Stephen Donald Jermy Gwyn  
August 21, 1995